

Conceptual Design of a Light-Aircraft Disc Brake

Dev Kumar, Amir Azzouz

▶ **To cite this version:**

Dev Kumar, Amir Azzouz. Conceptual Design of a Light-Aircraft Disc Brake. Independent research; original academic project at École Nationale Supérieure d'Arts et Métiers. 2026, pp.1-37. ⟨hal-05873383⟩

HAL Id: hal-05873383

https://hal.science/view/index/docid/5873383

Submitted on 20 Nov 2026

HAL is a multi-disciplinary open access archive for the deposit and dissemination of scientific research documents, whether they are published or not. The documents may come from teaching and research institutions in France or abroad, or from public or private research centers.

L'archive ouverte pluridisciplinaire **HAL**, est destinée au dépôt et à la diffusion de documents scientifiques de niveau recherche, publiés ou non, émanant des établissements d'enseignement et de recherche français ou étrangers, des laboratoires publics ou privés.



Copyright - All rights reserved

Conceptual Design of a Light-Aircraft Disc Brake

Load paths, clamped joints and
transient thermomechanical sizing

Dev KUMAR and Amir AZZOUZ

École Nationale Supérieure d’Arts et Métiers

Paris, France

Design study
Source design 2024–2025 · Numerical study 2026

Abstract

This design study examines a hydraulic disc brake for a 685 kg light aircraft. The technical dossier specifies a maximum rotor diameter of 125 mm, while its CAD drawing shows 160 mm. A common emergency-stop scenario is used to compare these envelopes, including bearing reactions, axle strength, clamped interfaces, pad friction and rotor temperature. At an initial ground speed of 53 m/s and a constant deceleration of 4 m/s², 400 N of residual thrust raises the brake work to 551 kJ per wheel. Using the unloaded radius shown on the assembly drawing gives 261 N·m per wheel. For an assumed rotor heat share of 0.80, the single-node model predicts peak bulk temperatures of 330 °C for the drawn rotor and 534 °C for a 125 mm rotor of comparable solid fraction. A two-node model raises those peaks at the friction track to 390 °C and 579 °C, respectively. Even the solid 125 mm envelope gives a track-node peak of 506 °C under the same assumptions. At the specified 280 bar, the 125 mm case also requires a pad friction coefficient of at least 0.180 in the idealised caliper model. The results identify the heat capacity, hot friction and load-path measurements needed for the next design iteration.

Keywords Light aircraft, disc brake, tapered roller bearings, bolted joint, hydraulic caliper, transient heat transfer.

Résumé

Cette étude de conception examine un frein à disque hydraulique pour un avion léger de 685 kg. Le cahier des charges limite le diamètre à 125 mm alors que le plan CAO indique 160 mm. Les deux enveloppes sont comparées sous le même scénario de freinage, du transfert de charge au dimensionnement de l’étrier et à l’échauffement du disque. À 53 m/s et 4 m/s², une poussée résiduelle de 400 N porte le travail de freinage à 551 kJ par roue. Le rayon hors charge du plan correspond à 261 N·m par roue. Pour une fraction de chaleur reçue par le disque de 0,80, les températures moyennes maximales simulées sont de 330 °C pour le disque dessiné et de 534 °C pour un disque de 125 mm de fraction pleine comparable. Les pics au nœud de piste atteignent respectivement 390 et 579 °C. La version pleine de 125 mm atteint encore 506 °C au nœud de piste sous les mêmes hypothèses. Le modèle d’étrier donne un coefficient de frottement minimal de 0,180 à 280 bar pour le disque de 125 mm. Ce calcul repère les données à mesurer pour arbitrer entre encombrement, capacité thermique et couple de freinage à chaud.

Mots-clés Avion léger, frein à disque, roulements coniques, assemblage vissé, étrier hydraulique, transfert thermique transitoire.

Nomenclature

Symbol	Definition
m, v_0, a	Aircraft mass, initial speed, imposed deceleration
F_t, F_b, T_w	Residual thrust, total brake force, wheel torque
R, s_s, t_s	Rolling radius, stop distance and duration
φ, η, μ_t	Static braked-wheel load share, height/wheelbase ratio, tire friction
F_a, F_r	Axial and radial resultant on a bearing
L_e, ℓ, χ	Bearing effective span, moment arm, axle torque fraction
p, A_p, μ_p	Hydraulic pressure, piston area, pad friction

Symbol	Definition
D, b, M_d	Disc diameter, envelope thickness, rotor mass
β, c_p, h, A	Rotor heat fraction, specific heat, coefficient and heat exchange area
T, T_a, T_k	Temperature, ambient, absolute scale (K)
T_s, T_c, G_{sc}	Track-node and core temperatures, thermal coupling
ε, σ_{SB}	Emissivity and Stefan–Boltzmann constant
P_0, F_0	Initial bearing-pair preload, clamp per fastener

Contents

Abstract 1
Résumé 1
Nomenclature 2
1. Design question and configuration 3
1.1 Design brief 3
1.2 Diameter discrepancy and configurations studied 3
1.3 Evidence and approach 4
2. Braking mission and wheel loads 4
2.1 Longitudinal equilibrium 4
2.2 Torque at the hub and corner-load imbalance 5
2.3 Braked-axle load and adhesion 6
2.4 Deceleration as an energy trade-off 6
3. Wheel-end architecture and bearings 6
3.1 Architecture and service access 6
3.2 Signed reactions with load position 8
3.3 External thrust, induced axial load and preload 9
3.4 Dynamic life and static capacity 10
4. Axle and torque-transmission joints 12
4.1 Sizing the load-bearing section 12
4.2 Twist and deflection 12
4.3 Stepped geometry and local stress 13
4.4 Clamped joints between rotor, hub and rim 15
5. Floating caliper and friction track 17
5.1 Clamp force and available torque 17
5.2 Effective pad radius 17
5.3 Pressure envelope and hot friction 18
5.4 Actuation and return 20
6. Thermal modelling and design sizing 20
6.1 Rotor mass and energy scale 20
6.2 Spatially averaged transient temperature 21
6.3 Track and core temperatures 21
6.4 Reference temperatures and sensitivity 23
6.5 Deceleration and inverse sizing 25
6.6 Numerical verification and model identification 28
7. Engineering disposition and verification 28
7.1 Conditional selection 28
7.2 Verification sequence 28
7.3 Conclusion 30
References 30
Appendix A. Source dossier and assembly sequence 31
Appendix B. Reproducible numerical model 32
B.1 Files and environment 32
B.2 Closed form in the linear thermal limit 32
B.3 Thermal energy closure 33
Appendix C. Technical drawings 33
Appendix D. Theory supplement 33

Theory boxes
Box 2.1 Ground-roll dynamics and adhesion 7
Box 3.1 Bearing contact, load zone and preload 11
Box 4.1 Axle strength, deflection and fatigue 14
Box 4.2 Torque–preload and joint stiffness 16
Box 5.1 Pad wear, hot friction and squeal 19
Box 6.1 Heat partition and surface temperature 22
Box 6.2 Thermal network, convection, radiation 24
Box 6.3 Repeated stops and identifiability 27
Box 7.1 Uncertainty and global sensitivity 29

1. Design question and configuration

1.1 Design brief

The technical dossier describes a wheel-end brake based on a coaxial disc, a floating caliper and a pair of opposed tapered roller bearings [1]. The brake must fit a predefined rim and tire and be serviceable when the wheel is removed. This study examines whether the architecture can be carried forward within the specified diameter, under one common braking scenario. The calculations form a preliminary design screen for the aircraft ground roll and the brake assembly.

The brief sets the aircraft mass at 685 kg, the initial speed at 53 m/s and the maximum deceleration at 4 m/s². It places brakes on two rear wheels, with two engines each supplying 200 N of opposing residual thrust during the stop. The 260 mm dimension refers to the rim outside diameter. Wheel torque depends on the effective tire rolling radius under load, which has to be established separately. Table 1.1 identifies the project inputs and their status.

Table 1.1 – Requirements and archived design inputs. Page numbers refer to the original technical dossier [1].

Quantity	Value	Status
Mass and ground speed	685 kg, 53 m/s	Design scenario, p. 3
Maximum deceleration	4 m/s²	Operating limit, p. 3
Residual thrust	400 N	Two × 200 N, p. 3
Braked wheels	Two rear	Design brief, p. 3
Rim outside diameter	260 mm	Packaging input, p. 3
Disc diameter	≤125 mm	Packaging requirement, p. 3
Disc family drawn	160 × 22 mm	Diameter and total height, p. 18
Piston and pressure	13 mm, 280 bar	Piston radius and line pressure, p. 13
Disc mass and temperature	2.791 kg, 450 °C	Note value and study reference, p. 12

The task is organised around four interfaces. The tire and runway set the longitudinal force that can be supported. The rotor and caliper deliver the corresponding torque. The hub, bearings, axle and clamped joints carry distinct components of that load. The transient partition of energy between the disc, pads and surroundings determines whether a cold or warm stop approaches the thermal reference.

1.2 Diameter discrepancy and configurations studied

The brief gives a 125 mm maximum outer disc diameter. The rotor drawing instead gives Ø160 mm and 22 mm overall thickness, with a Ø32.10 mm centre bore and a stepped feature of Ø50.10 mm. The two diameters differ by 35 mm, or 17.5 mm in radial reach. The assembly and rotor drawings are dated 9 January 2025 and reproduced as Plates C.1–C.3.

Three alternatives are evaluated in Table 1.2. The drawn configuration uses the reported mass. The capped configuration with comparable relief transfers the ratio of reported mass to solid-annulus mass from the drawn design. The solid 125 mm envelope gives a second capped case that maximises the retained mass for the common material, bore and thickness. Both capped cases are geometric models. Drawing release requires a packaging check and a consistent revision of the rotor, carrier and caliper.

Table 1.2 – Design alternatives evaluated under the same stop and a 22 mm total height.

Case	Ø (mm)	Mass (kg)	Role
Drawn	160	2.791	Geometry and note mass
Capped, comparable relief	125	1.658	Scaled solid fraction
Capped, solid bound	125	1.980	Unrelieved envelope upper mass

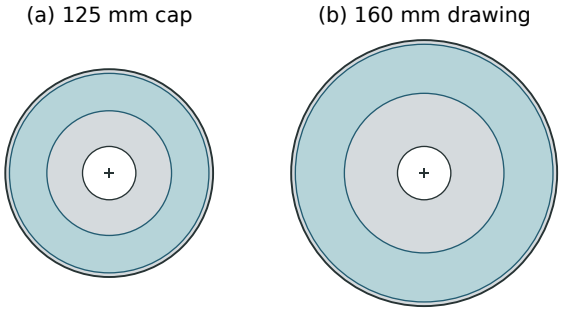

Figure 1.1 – Cross-sectional footprint in the disc plane for the two outer diameters. The coloured ring is the assumed friction track used in the caliper comparison. Drawn for this report. Holes and registers are shown on Plate C.3.

1.3 Evidence and approach

The original calculations and CAD drawings [1] supply the architecture and project values. Appendix A gives the link to each design sheet and preserves its assembly sequence. Where the dossier gives an ambiguous or inconsistent value, the calculation that uses it and the corresponding sensitivity are shown. Material properties, wheel-load shares, pad friction and heat-transfer coefficients introduced here are modelling inputs. Python solves the thermal balances and produces the parametric comparisons. Section 6 and Appendix B give the numerical checks and execution details.

The load cases are based on a longitudinal stop at a prescribed deceleration. Side loads, aircraft pitch transients, runway unevenness, aerodynamic forces, the details of the wheel assembly inertia, and component fatigue spectra require separate inputs. A civil-aircraft certification programme would define and substantiate brake energy absorption and operating conditions for the applicable basis. The EASA normal-category specification provides an example [2]. The calculations here support the stage at which packaging and component requirements are decided.

2. Braking mission and wheel loads

2.1 Longitudinal equilibrium

Use a ground-fixed frame with the forward direction positive. Let a>0 denote the deceleration magnitude, F_t the forward residual thrust and F_b the sum of the resisting tire forces at the two braked wheels. The reference case neglects drag and rolling resistance. Integrating the resulting equations from v_0 to zero gives

$$m\dot{v} = F_t - F_b = -ma \qquad F_b = ma + F_t, \qquad v(t) = v_0 - at \tag{2.1}$$

$$t_s = \frac{v_0}{a}, \qquad s_s = \frac{v_0^2}{2a}. \tag{2.2}$$

The elapsed time and distance start at brake application. A delay between touchdown and brake application would add its own distance. Using the maximum deceleration throughout obtains the shortest stop in this constant-force family. Feasibility depends on tire grip and the brake torque available as pressure and temperature vary.

Multiply the force balance by speed and integrate in time. For an equal share across the two brakes,

$$W_{b,w} = \frac{F_b s_s}{2} = \frac{1}{2}\left(\frac{m v_0^2}{2} + F_t s_s\right). \tag{2.3}$$

At the reference point the translational energy is 962.1 kJ and the engines add 140.5 kJ during the braking distance. Each brake accounts for 551.3 kJ. The useful comparison with the mass of the rotor comes after this energy has been distributed between the two wheel ends and partitioned among the brake components. With three landing-gear wheels the partition still follows the two actuated wheels in this configuration.

Table 2.1 – Reference stop under symmetric braking and constant residual thrust.

Output	Value
Total brake force (N)	3140
Tangential force per wheel (N)	1570
Braking time (s)	13.25
Distance from brake application (m)	351.1
Initial translational energy (kJ)	962.1
Work of residual thrust (kJ)	140.5
Brake work per wheel (kJ)	551.3
Initial power per wheel (kW)	83.21

The initial braking power on one wheel is 83.21 kW. The idealised power falls linearly with speed and has mean 41.61 kW. More precisely, the source rate and the work accumulated from time zero are

$$P_w(t) = \tfrac{1}{2} F_b (v_0 - a t)$$
$$W_w(t) = \tfrac{1}{2} F_b \left(v_0 t - \tfrac{1}{2} a t^2\right) \qquad (2.4)$$
$$0 \le t \le t_s.$$

Figure 2.1 gives the time profile needed for the thermal balance. At brake application in a cold stop, heat generation is highest and the temperature difference driving convection and radiation is zero.

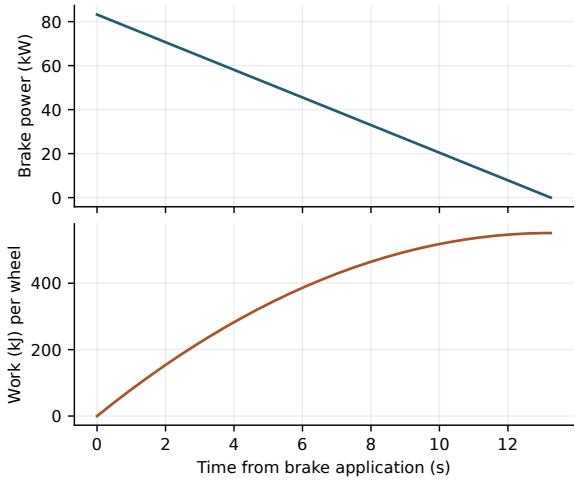

Figure 2.1 – Power and cumulative brake work per wheel at the reference stop. Python calculation from Eqs. (2.1)–(2.4).

2.2 Torque at the hub and corner-load imbalance

Neglecting wheel angular inertia and assuming rolling without slip, v=ω R. The traction force and brake torque at each ideal wheel satisfy

$$T_w = \frac{F_b R}{2}, \qquad T_w \omega = P_w. \qquad (2.5)$$

The dossier's 204 N·m per wheel is reproduced by the 130 mm rim radius. The 166.04 mm radius marked on Plate C.2 describes the unloaded geometric tire envelope. Using it as a comparison point gives 260.7 N·m, or 28% more. Taking 150 mm as an intermediate radius gives 235.5 N·m. Measure the loaded tire radius before setting a component torque requirement.

Table 2.2 – Wheel radius sensitivity at the reference force.

Radius (mm)	Torque (N·m)	Interpretation
130.00	204.1	Rim radius, original check
150.00	235.5	Intermediate case
166.04	260.7	Unloaded drawing radius
175.00	274.8	Upper sensitivity case

The kinetic energy of the rotating parts adds a separate term. For a combined wheel and rotor inertia I_w for one wheel and constant R, its initial rotational energy and contribution to the hub torque are

$$E_{\mathrm{rot},w} = \frac{I_w v_0^2}{2R^2}, \qquad \Delta T_w = I_w \frac{a}{R}. \qquad (2.6)$$

The additional energy follows by integrating $\Delta T_w \omega$ to zero speed. It is kept symbolic because an inertia value for the full rotating assembly is absent. If a fraction λ of the total force is assigned to the more loaded brake, wheel force, work and torque scale by 2λ relative to the symmetric case. At λ=0.60, that wheel sees 1,884 N, 662 kJ and about 313 N·m at the same geometric radius. This is a sensitivity case. Asymmetric yaw and the remaining

friction capacity must be included when assigning a design value.

2.3 Braked-axle load and adhesion

Let φ be the static fraction of weight on the braked rear wheels, h_g the height of the centre of gravity and L_w the wheelbase. A first moment balance about the static load line yields a rear load loss $h_g F_b/L_w$ when thrust acts through the centre of gravity, pitch is quasi-static and aerodynamic contributions are zero. The ground-level longitudinal forces are consolidated into F_b. With $\eta=h_g/L_w$,

$$N_R = \phi mg - \eta F_b, \qquad N_F = mg - N_R. \tag{2.7}$$

The brake demand is admissible in this ideal model when $F_b \le \mu_t N_R$. Substituting the load-transfer equation gives the total force and deceleration bounds

$$F_{b,\max} = \frac{\mu_t \phi mg}{1+\eta\mu_t}, \qquad a_{\max} = \frac{F_{b,\max} - F_t}{m}. \tag{2.8}$$

The position and load distribution of the actual aircraft have to replace the illustrative φ=0.80 and η=0.22. These values yield 4.685 kN normal force on the rear axle and a minimum tire/runway coefficient of 0.670 for the reference stop. Figure 2.2 plots the dependence on rear share and grip. A shift in loading towards the forward wheel or reduced grip moves the system towards a smaller reachable deceleration. For a single tire, simultaneous side force can be represented initially by the friction-circle bound $F_x^2+F_y^2 \le (\mu_t N)^2$. Its use requires individual normal forces. The pad coefficient μ_p in Section 5 describes a different interface.

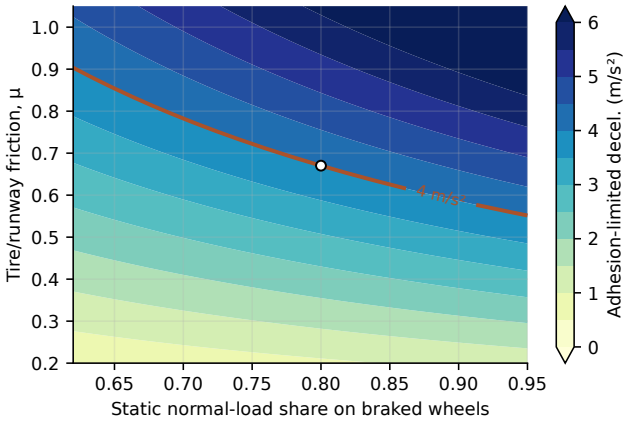

Figure 2.2 – Adhesion-limited deceleration in the quasi-static model at η=0.22. The orange contour is the 4 m/s² reference. The marker combines the illustrative load distribution and its required grip.

2.4 Deceleration as an energy trade-off

Reducing the commanded deceleration spreads the event over more time and lowers the initial mechanical power. Constant residual thrust, however, supplies more work over the longer distance. For example, at 2 m/s² the application-to-stop distance is 702.3 m, the initial power is 46.91 kW per wheel, and the work is 621.5 kJ per wheel. At a fixed rotor heat share, total heat input rises with this additional work. Thermal consequences depend on the cooling over that longer interval, as calculated in Section 6.

3. Wheel-end architecture and bearings

3.1 Architecture and service access

The original methodology begins with bearing reactions, service access and packaging, then compares caliper positions and bearing arrangements before sizing the pair preload, joints and component geometry [1]. The selected architecture puts a floating caliper on the inboard side, so the frequently serviced wheel can be approached from outside without routing the caliper around the tire. The coaxial wheel-disc assembly runs on two opposed tapered roller bearings. Plate C.1 gives the arrangement and parts list.

Box 2.1 Ground-roll dynamics, adhesion with lift and the work of the stop

Theoretical complement to Sections 2.1–2.4. Values computed by brake_theory.py (Appendix D); aerodynamic coefficients are illustrative.

Extended longitudinal model

Adding drag, lift L and rolling resistance C_{rr} to (2.1),

$$m\dot{v} = F_t - F_b - \tfrac{1}{2}\rho C_D S\, v^2 - C_{rr}\,(mg - L), \qquad L = \tfrac{1}{2}\rho C_L S\, v^2. \tag{B2.1}$$

At an imposed constant deceleration the brakes supply only the part of $ma + F_t$ not taken by drag and rolling resistance. Since $ds = v\,dt$ and $v = v_0 - at$, $\int_0^{s_s} v^2 ds = \int_0^{t_s} v^3 dt = v_0^4/(4a)$, hence

$$E_D = \frac{\rho C_D S\, v_0^4}{8a}, \qquad E_{rr} \le C_{rr}\, mg\, s_s. \tag{B2.2}$$

With $\rho = 1.225\,\mathrm{kg/m^3}$, $E_D = 90.6\,\mathrm{kJ}$ for $C_D S = 0.3\,\mathrm{m^2}$ and 151.0 kJ for $0.5\,\mathrm{m^2}$, 8.2% and 13.7% of the 1102.5 kJ absorbed by both brakes. Rolling resistance at $C_{rr} = 0.02$ adds at most 47.2 kJ, so Table 2.1 is conservative for brake work.

Why the maximum deceleration is optimal

For any admissible deceleration law $a(v) \le a_{\max}$ the distance is $s_s = \int_0^{v_0} v\,dv/a(v)$, which is minimised pointwise by $a(v) = a_{\max}(v)$. The brake work per wheel,

$$W_{b,w} = \tfrac{1}{2}(\tfrac{1}{2}mv_0^2 + F_t\, s_s), \tag{B2.3}$$

is minimised by the same law because thrust works over the distance. For constant a, $\partial W_{b,w}/\partial a = -F_t v_0^2/(4a^2) = -17.6\,\mathrm{kJ}$ per $\mathrm{m/s^2}$ at $4\,\mathrm{m/s^2}$. Distance, duration and heat all favour the largest deceleration that adhesion and torque allow (the bang-bang law of Pontryagin's principle); only the peak power $\tfrac{1}{2}(ma + F_t)v_0$ grows with a.

Adhesion with lift

With lift, (2.7) becomes $N_R(v) = \phi\,(mg - L(v)) - \eta F_b$, and $F_b \le \mu_t N_R$ gives the speed-dependent limit

$$a_{\mathrm{adh}}(v) = \frac{1}{m}\Big[\frac{\mu_t\phi\,(mg - \tfrac{1}{2}\rho C_L S\, v^2)}{1 + \eta\mu_t} - F_t\Big]. \tag{B2.4}$$

The reference stop is feasible at brake application only if

$$C_L S \le \frac{mg - F_b(1/\mu_t + \eta)/\phi}{\tfrac{1}{2}\rho v_0^2}, \tag{B2.5}$$

which gives $0.552\,\mathrm{m^2}$ ($L \le 950\,\mathrm{N}$) at $\mu_t = 0.8$ and $0.145\,\mathrm{m^2}$ at $\mu_t = 0.7$. At $\mu_t = 0.6$ the right-hand side is negative: the stop is infeasible even without lift, in line with the 0.670 of Section 2.3.

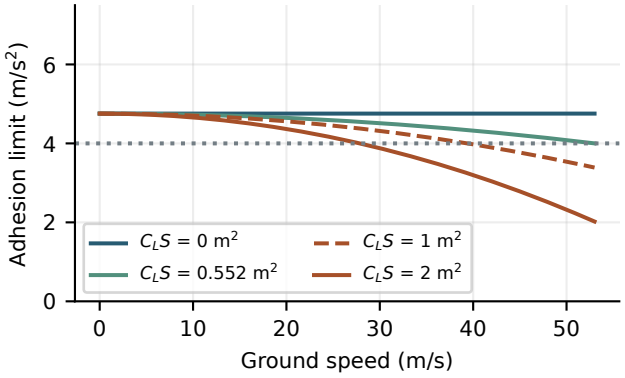

Adhesion-limited deceleration (B2.4) at $\mu_t = 0.8$, $\phi = 0.80$, $\eta = 0.22$. Dotted line: $4\,\mathrm{m/s^2}$ reference.

For an illustrative $C_L S = 2\,\mathrm{m^2}$ the limit at 53 m/s is $2.02\,\mathrm{m/s^2}$, and $4\,\mathrm{m/s^2}$ becomes available only below 27.8 m/s. Integrating $\dot{v} = -\min(a_{\max}, a_{\mathrm{adh}}(v))$ gives a stop of 15.3 s over 447.7 m, with 570.6 kJ per wheel (+3.5%). The lift remaining at the start of the roll, not the brake, can then set the stop.

Slip dynamics of the braked wheel

A tire force requires the slip $\kappa = (v - \omega R)/v$. With $I_w\dot{\omega} = N\mu(\kappa)R - T_b$,

$$\dot{\kappa} = -\frac{R}{v}\,\dot{\omega} + (1 - \kappa)\frac{\dot{v}}{v}. \tag{B2.6}$$

Linearising about an equilibrium $\mu(\kappa_0) = T_b/(NR)$ and holding v frozen gives $\delta\dot{\kappa} = -\delta\kappa/\tau_\kappa$ with

$$\tau_\kappa = \frac{I_w v}{NR^2\mu'(\kappa_0)}. \tag{B2.7}$$

It is stable on the rising branch of a curve such as Pacejka's $\mu = D\sin\{C\arctan[B\kappa - E(B\kappa - \arctan B\kappa)]\}$ and unstable beyond its peak, where the wheel locks. Without anti-skid modulation the torque must stay below $NR\mu_{\mathrm{peak}}$ with margin; $\mu(\kappa)$ belongs with the corner loads of Table 7.2.

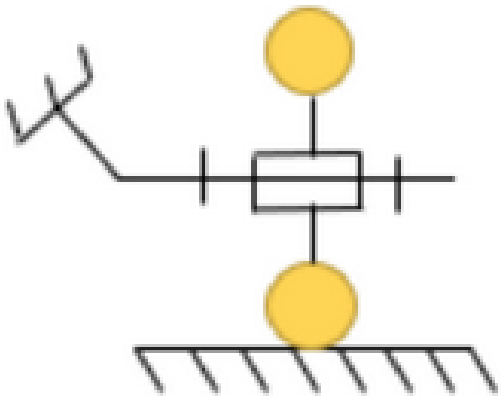

Figure 3.1 – Original schematic of airframe, wheel and brake connections [1, p. 5]. The labels identify the aircraft and brake in French.



Figure 3.2 – Original exploded CAD model of the wheel-end concept [1, p. 6]. The large outer element is the wheel. The carrier, bearing stack and caliper occupy the inboard assembly.

The global load paths are different for force and torque. The vertical and longitudinal contact forces go through the wheel and hub into the bearing stack and then to the fixed support. At the pad contacts the rotor torque is reacted by the caliper. The caliper bracket connects to the airframe-side support. How much of that moment enters a given axle section depends on the support interfaces. The assembly view is a basis for locating the paths. A stiffness model or physical free-body cut is required to assign the moment to each section.

The opposed back-to-back pair, termed an O arrangement in the dossier, separates the effective load centres compared with a closer direct arrangement for a given bearing stack. Increasing the effective span lowers the reaction difference for an imposed tilting moment. Assembly constraints include access to the nuts and caps, accurate shoulder and spacer lengths and a verified preload or endplay setting.

3.2 Signed reactions with load position

Let L_e be the effective distance between rollers' load centres A and B. Let ξ be the position of a transverse force F measured from A in the same plane. Taking moments about A and imposing $R_A+R_B=F$ gives

$$R_A = F\left(1-\frac{\xi}{L_e}\right), \qquad R_B = F\frac{\xi}{L_e}. \tag{3.1}$$

The archived midspan idealisation is shown in Fig. 3.3. At $\xi=L_e/2$, each support carries F/2. The word “cantilever” in the project also describes the attachment to the airframe. Wheel load position is measured independently from the centres of pressure. For a force a distance $e=\xi-L_e>0$ beyond B, the corresponding reactions are



Figure 3.3 – Midspan loading assumption in the original functional sketch [1, p. 5].

$$R_A = -F\frac{e}{L_e}, \qquad R_B = F\left(1+\frac{e}{L_e}\right). \tag{3.2}$$

The negative sign means reversal of the support reaction. It enters the bearing and housing analysis through its direction and magnitude. In an overhung configuration the nearest support can see a larger radial load than the applied force. For the reference

braking and load-transfer cases, neglecting side force and using equal wheel shares gives

$$F = \frac{1}{2}\sqrt{F_b^2 + N_R^2}\,. \tag{3.3}$$

Here F=2.82 kN. With a 45 mm span and the wheel load 15 mm beyond B, the radial reactions are −0.94 and +3.76 kN. Centring the same load yields 1.41 kN per bearing. This explains why the effective position and the bearing span matter more than dividing the aircraft force equally. The 45 mm and 15 mm dimensions are sensitivity inputs. Actual load centres should be computed from the chosen bearing data and the assembly geometry.

Table 3.1 – Equivalent static reactions for a 2.82 kN radial wheel load. Span between centres is 45 mm in both examples.

Load location	A (kN)	B (kN)
At midspan	+1.41	+1.41
15 mm beyond B	−0.94	+3.76

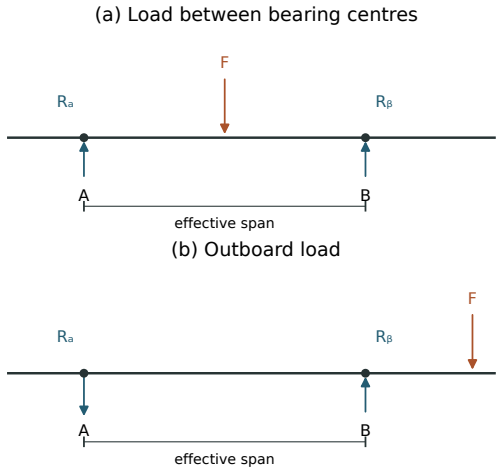

Figure 3.4 – Free-body definitions for the two load locations. The load reversal in panel (b) follows from equilibrium. Drawn for this report.

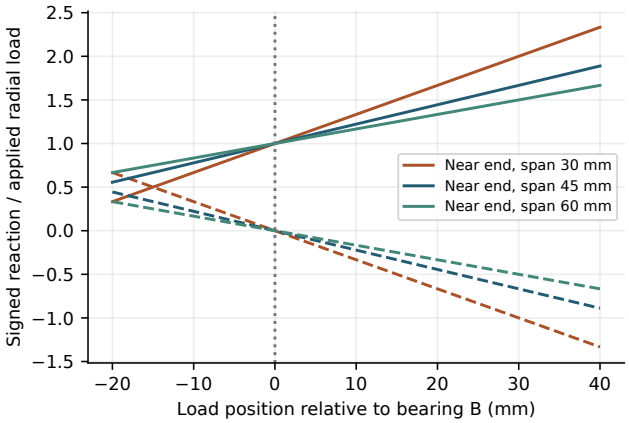

Figure 3.5 – Sensitivity of signed bearing reactions to load location and effective span. Solid lines denote B, dashed lines A. The abscissa is measured from B.

3.3 External thrust, induced axial load and preload

The 2,740 N in the original worksheet is 685 × 4 and acts along the aircraft longitudinal axis. The axle is transverse to that direction. An independent lateral tire force or a geometric component along the axle is needed to establish external axial loading. Tapered rollers also transmit an internal axial force under radial load because the contact lines are oblique. The catalogue rule $F_{a,ind}=F_r/(2Y)$ can be used as part of the pair equations in SKF Table 7 for single-row bearings adjusted close to zero clearance without preload [3].

The worksheet assumes F_r=456.7 N and Y=1.6. Those inputs give 142.7 N under the quoted relation. The worksheet records 357 N and 3,097 N, which reflect the arithmetic and load-direction discrepancies. The 2,740 N preload in the worksheet and the 5,329 N printed on the assembly sheet are retained below as separate sensitivity inputs. The latter annotation should be reconciled with the tightening and spacer definitions on the drawing.

To separate the role of preload from the catalogue calculation, consider two opposing axial springs with the same tangent stiffness k_a near the initial contact load P_0. An external axle force $F_a \geq 0$ perturbs the displacement by u. With both contacts closed, equilibrium and compatibility give

$$\begin{aligned} F_a &= 2k_a u, \\ P_{\pm} &= P_0 \pm \tfrac{1}{2}F_a. \end{aligned} \tag{3.4}$$

The relieved bearing reaches zero at $F_a=2P_0$. Beyond that value this ideal unilateral model gives $P_-=0$, $P_+=F_a$. Real bearings have nonlinear force–displacement curves and radial–axial coupling. The simplified relation isolates the consequence of a preload assumption, as illustrated in Fig. 3.6. At 2,740 N of initial pair load the equal-spring model opens at 5.48 kN, while at 5,329 N it opens at 10.66 kN. An allowable preload is also limited by bearing contact stress, friction and thermal effects.

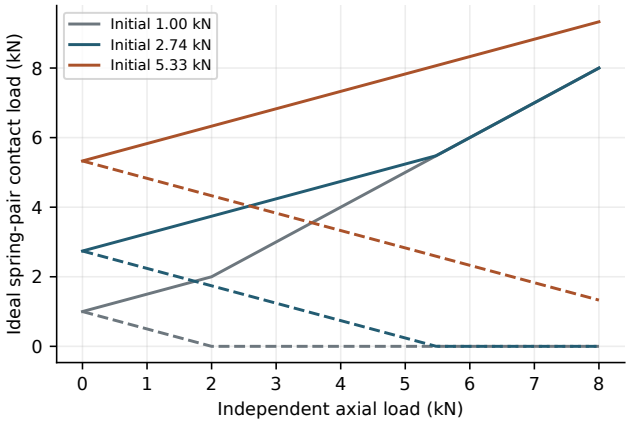

Figure 3.6 – Contact loads for the preloaded axial spring pair. Solid lines show the loaded contact and dashed lines the relieved contact. The applied axial force is an independent input.

Plate C.2 records axial and radial spacer stiffness values of 159 and 157 MN/m and a displacement of 0.1 mm. If the axial displacement were carried by the spacer alone, 0.1 mm would correspond to 15.9 kN. The two nominal loads 2,740 N and 5,329 N would correspond to 17.2 and 33.5 µm, respectively. In an assembly the effective squeeze is distributed between bearing contacts, spacer and support structure. An ideal series approximation is

$$\frac{1}{k_{\mathrm{eq}}} = \frac{1}{k_{\mathrm{sp}}} + \frac{1}{k_{\mathrm{A}}} + \frac{1}{k_{\mathrm{B}}} + \frac{1}{k_{\mathrm{h}}}. \tag{3.5}$$

The effective preload changes with manufacturing tolerances and differential thermal expansion. A preload update can be written locally as $\Delta P \simeq k_{\mathrm{eq}}\Delta u$ once stack dimensions, temperatures and their signed changes are established. The force, displacement and tightening variables therefore need a common reference condition.

3.4 Dynamic life and static capacity

For an identified tapered roller bearing, the basic ISO 281 rating life is expressed in revolutions using the equivalent dynamic load P and dynamic rating C [4]. The exponent is 10/3. The basic model is associated with 90% reliability under the standard's reference assumptions.

$$L_{10} = 10^6 \left(\frac{C}{P}\right)^{10/3}, \qquad P = XF_r + YF_a. \tag{3.6}$$

The second relation denotes a catalogue branch for combined load. The coefficients, branch threshold, pair-specific axial reaction and static rating C_0 must be taken from the selected bearing. With load blocks of n_j rotations and equivalent loads P_j, a basic duty approximation is

$$P_{\mathrm{eq}} = \left(\frac{\sum_j n_j P_j^{10/3}}{\sum_j n_j} \right)^{3/10}. \tag{3.7}$$

The static check uses the equivalent static load and static safety factor. It covers landed and parked conditions, which may set high forces at near-zero speed. A full selection also considers fits, contamination, lubrication, radial clearance, thermal growth, load reversal, sealing and fatigue under the actual duty. Catalogue life depends on the selected bearing and the corner-load duty envelope.

Box 3.1 Contact mechanics, load distribution and preload of the tapered-roller pair

Theoretical complement to Sections 3.2–3.4. Integrals and factors computed by brake_theory.py (Appendix D); bearing geometry remains to be taken from the selected catalogue part.

Hertzian line contact

A roller of effective length l pressed by a load Q against its raceway forms a strip of half-width b. With the load per unit length $w = Q/l$, the reduced radius $1/R' = 1/R_1 + 1/R_2$ and the contact modulus $1/E^* = (1-\nu_1^2)/E_1 + (1-\nu_2^2)/E_2$, the plane-strain solution gives

$$b = \sqrt{\frac{4wR'}{\pi E^*}}, \qquad p_0 = \frac{2w}{\pi b} = \sqrt{\frac{wE^*}{\pi R'}}. \tag{B3.1}$$

The largest shear stress, $0.30\,p_0$, lies at a depth of $0.78\,b$ below the surface. Rolling-contact fatigue starts there, and this subsurface origin underlies the Lundberg–Palmgren theory behind (3.6). The approach of a finite line contact has no closed Hertz form; Palmgren's fit, with δ in mm, Q in N and l in mm, is

$$\delta = 3.84\times10^{-5}\,\frac{Q^{0.9}}{l^{0.8}} \quad\Longrightarrow\quad Q = K\delta^{n},\ n = \tfrac{10}{9}. \tag{B3.2}$$

Load zone and induced thrust

For a single row with Z rollers at contact angle α and a load zone described by ε, the roller loads follow $Q(\psi) = Q_{\max}[1-(1-\cos\psi)/(2\varepsilon)]^{n}$ inside the zone. Summing the components over the zone $|\psi| \le \psi_l$, $\cos\psi_l = 1-2\varepsilon$, gives the Sjövall integrals,

$$F_r = ZQ_{\max}\cos\alpha\,J_r, \quad F_a = ZQ_{\max}\sin\alpha\,J_a,$$
$$\begin{bmatrix}J_r\\ J_a\end{bmatrix} = \frac{1}{2\pi}\int_{-\psi_l}^{\psi_l}\Big[1-\frac{1-\cos\psi}{2\varepsilon}\Big]^{n}\begin{bmatrix}\cos\psi\\ 1\end{bmatrix}d\psi, \tag{B3.3}$$

so that $F_a/F_r = \tan\alpha\,J_a/J_r$. Quadrature gives $J_r = 0.2448$ and $J_a = 0.3080$ at $\varepsilon = 0.5$, hence $J_a/J_r = 1.258$; the ratio rises to 1.538 at $\varepsilon = 0.8$ and 1.900 at $\varepsilon = 1$. The catalogue rule $F_{a,\mathrm{ind}} = F_r/(2Y)$, with $Y = 0.4\cot\alpha$, reads $F_a = 1.25\,F_r\tan\alpha$. It is therefore the half-loaded zone ($\varepsilon = 0.5$) of (B3.3), within 0.6%. With the worksheet's $Y = 1.6$ ($\tan\alpha = 0.25$), the 3.76 kN reaction of Table 3.1 induces 1.175 kN by the catalogue rule and 1.183 kN from (B3.3).

Nonlinear preload of the O pair

Let both rows follow (B3.2), be mounted with an initial approach δ_0 ($P_0 = K\delta_0^{n}$) and be displaced by u under an external force F_a:

$$F_{\pm} = K(\delta_0 \pm u)^{n}, \qquad F_a = F_+ - F_-. \tag{B3.4}$$

Equation (3.4) is the tangent of (B3.4) at $u = 0$, where the pair stiffness is

$$k_0 = \frac{2nP_0}{\delta_0} = 2nK^{1/n}P_0^{1-1/n} \propto P_0^{0.1}. \tag{B3.5}$$

Doubling the preload therefore raises the stiffness by only 7%, while contact stress and friction grow with it. The relieved row lifts off at $u = \delta_0$, where

$$F_{a,\mathrm{lift}} = K(2\delta_0)^{n} = 2^{10/9}P_0 = 2.160\,P_0. \tag{B3.6}$$

For the two recorded preloads this gives 5.92 kN and 11.51 kN, 8% above the 5.48 and 10.66 kN of the linear model. The linear model is therefore conservative for the opening load.

Reliability, duty and revolutions

The ISO 281 reliability factors follow from a three-parameter Weibull law of slope 3/2 with a minimum life of $0.05\,L_{10}$ [4]:

$$a_1(S) = 0.95\Big[\frac{\ln(1/S)}{\ln(1/0.9)}\Big]^{2/3} + 0.05. \tag{B3.7}$$

This gives 0.638, 0.366 and 0.248 for $S = 95$, 98 and 99%, the tabulated 0.64, 0.37 and 0.25. The equivalent load (3.7) is Miner's linear damage sum $D = \sum_j n_j/L_j \le 1$ with $L_j = (C/P_j)^{10/3}$. A wheel completes $s_s/(2\pi R) = 337$ revolutions during the reference stop, so 10^4 such stops amount to 3.4×10^6 revolutions. The duty is short and heavily loaded, which shifts the selection towards static capacity C_0, shock and preload retention rather than the basic rating life.

Thermal change of preload

Preload also depends on temperature through the stack. With a signed change $\Delta u_T = \sum_i \alpha_i L_i \Delta T_i$ of the axial stack length, (3.5) gives $\Delta P \simeq k_{eq}\Delta u_T$ before liftoff. Its sign for a hub heated by the rotor around a cooler axle depends on the arrangement and on the radial fits, so thermal soak belongs among the preload checks, with the histories of Section 6.

4. Axle and torque-transmission joints

4.1 Sizing the load-bearing section

The circular shaft equations are applied to candidate sections once the bending moment and torque in the section are specified. For a solid diameter d, the second moment of area I, polar moment J and bending section modulus W are

$$I=\frac{\pi d^4}{64},\quad J=\frac{\pi d^4}{32},\quad W=\frac{2I}{d}. \tag{4.1}$$

For an effective transverse load arm ℓ measured at the section and a torque fraction χ entering the axle, the reference inputs are $M=F\ell$ and $T=\chi T_w$. This parameterisation separates the wheel torque from the torque entering a particular solid section. For nominal stress and an elastic concentration factor on each mode,

$$\sigma_b=\frac{32M}{\pi d^3},\quad \tau=\frac{16T}{\pi d^3},\quad \sigma_{\mathrm{eq}}=\sqrt{(K_b\sigma_b)^2+3(K_t\tau)^2}. \tag{4.2}$$

Here K_b is a bending concentration factor and K_t a torsional concentration factor. The equivalent stress uses the von Mises expression for one normal stress and one shear stress. Solving $\sigma_{eq}\le\sigma_{adm}$ for d gives

$$d_\sigma=\left[\frac{16\sqrt{(2K_bM)^2+3(K_tT)^2}}{\pi\sigma_{\mathrm{adm}}}\right]^{1/3}. \tag{4.3}$$

The original torsion check states a 140 MPa limit and a factor of two. If 140 MPa is used as a uniaxial reference before that factor, 70 MPa is the admissible equivalent stress. Pure-torsion shear is then limited to $70/\sqrt{3}=40.4$ MPa. If instead 140 MPa is already a reduced uniaxial allowable derived from a 280 MPa property, the corresponding shear is 80.8 MPa. The basis for the “S280” label, material condition and factor should be fixed together. The sensitivity study uses 70 MPa in equivalent stress. This value serves to compare geometries and force paths.

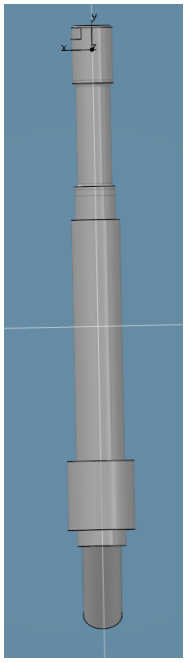

Figure 4.1 – Sectioned shaft schematic from [1, p. 8]. Plate C.2 gives the drawing views of the assembled axle.

4.2 Twist and deflection

The local angle gradient in each constant section is $\theta'=T/(GJ)$. Dividing the original total rotation equation by the length is essential when the constraint is an angle per metre. For the stated $\theta'_{\mathrm{lim}}=0.25°/\mathrm{m}$, use $0.25\pi/180$ rad/m. In a uniform cantilever segment of length ℓ, the transverse end deflection follows from integrating $EIy''=M(x)$ with zero displacement and slope at the clamp. The three resulting sizing equations are

$$\theta'=\frac{T}{GJ},\quad d_\theta=\left[\frac{32|T|}{\pi G\theta'_{\mathrm{lim}}}\right]^{1/4}, \tag{4.4}$$

$$\delta=\frac{F\ell^3}{3EI},\quad d_\delta=\left[\frac{64F\ell^3}{3\pi E\delta_{\mathrm{lim}}}\right]^{1/4}, \tag{4.5}$$

$$d_{\mathrm{req}} = \max(d_\sigma, d_\theta, d_\delta). \tag{4.6}$$

The twist for an entire stepped shaft is the integral of the gradient over its segments. End deflection under an overhung load in the actual assembly also includes bearing and support compliance. Equation (4.5) uses an ideal clamp as a local comparison. Using E=210 GPa, 2.82 kN and an ideal 50 mm cantilever, the uniform 32.1 mm section gives 10.7 µm. The maximum acceptable deflection depends on the clearance at the pads, bearings and rotating seals. Its verification requires the displacement of the complete stack and its tolerance chain.

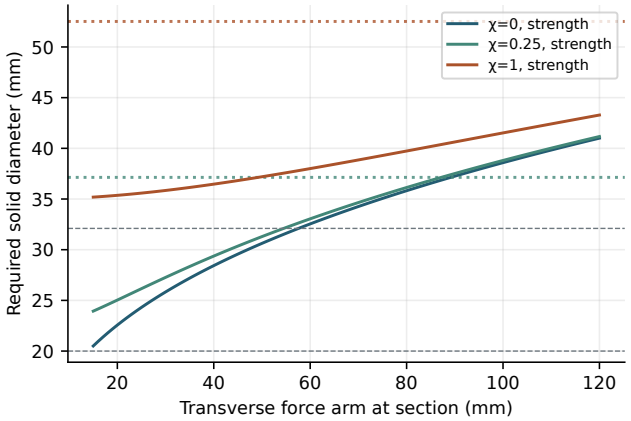

Figure 4.2 – Diameter screen for three axle torque fractions at F=2.82 kN. Solid curves are equivalent-stress diameter limits with K_b=1.4 and K_t=1.3. Dotted lines are twist limits. Dashed lines mark archived step diameters for scale.

Table 4.1 – Shaft screening at a 50 mm force arm and a 70 MPa equivalent-stress reference. The angle-gradient requirement was taken from [1].

Axle torque share	Strength diameter (mm)	Twist diameter (mm)	Stress at 32.1 mm (MPa)
0	30.6	—	60.8
0.25	31.3	37.1	64.9
1	37.2	52.5	108.9

Figure 4.2 shows the relative effects of force arm and transmitted torque. At a 50 mm arm with χ=0, the calculated strength diameter is 30.6 mm. When all 260.7 N·m enters the model section it rises to 37.2 mm, and the inherited twist criterion gives 52.5 mm. If a quarter of that torque enters the section, strength requires 31.3 mm and the twist criterion gives 37.1 mm. Doubling the arm at fixed radial force scales the bending-only diameter by $2^{1/3}$. The twist diameter scales with the fourth root of torque. The results therefore indicate which free-body cuts and support measurements would narrow the apparent design range.

4.3 Stepped geometry and local stress

The original note reports two shoulders. The first joins Ø16 and Ø20 mm with a 2 mm fillet and lists a factor of 1.0 and 195 MPa. The second joins Ø20 and Ø32.1 mm with a 0.5 mm fillet and lists 1.2 and 270 MPa. Both quoted stresses exceed 140 MPa. The governing load combination and derivation of those stresses are unspecified, so the records are retained as archived checks. A stress estimate from M/W uses the section modulus. Each shoulder has to be evaluated on its own section geometry, local force path, combination of bending and torsion, and material condition.

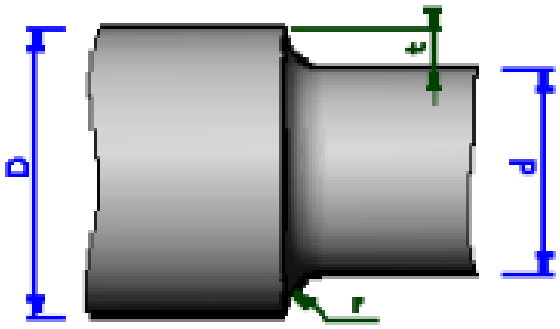

Figure 4.3 – Archived shoulder geometry and concentration-factor illustration [1, p. 10]. The source calculation supplies the shoulder dimensions discussed in the text.

For fatigue, the relevant amplitudes depend on whether an axle section rotates with the load and whether braking torque is intermittent. With linear-elastic stresses and an appropriate fatigue basis, a preliminary combined mean and alternating stress constraint can use $\sigma_a/S_e + \sigma_m/S_u \le 1/n_f$. Here S_e is a corrected endurance value, S_u the tensile strength and n_f the fatigue factor. These quantities, the finish and notch sensitivity would need to be specified before applying the expression. The available static calculation can locate candidate checks in fillets, threads and interfaces.

Box 4.1 Multiaxial strength, short-beam deflection and fatigue of a stationary axle

Theoretical complement to Sections 4.1–4.3. Values computed by brake_theory.py (Appendix D) at $F = 2.82\,\mathrm{kN}$, $\ell = 50\,\mathrm{mm}$ and $T_w = 260.7\,\mathrm{N{\cdot}m}$; the steel strength in the fatigue example is illustrative.

Equivalent-stress criteria

At the critical surface point of a circular section, the bending stress σ and the torsional shear τ give principal stresses $\sigma_{1,2} = \sigma/2 \pm \sqrt{\sigma^2/4 + \tau^2}$, $\sigma_3 = 0$. The distortion-energy (von Mises) and maximum-shear (Tresca) measures are

$$\sigma_{\mathrm{vM}} = \sqrt{\sigma^2 + 3\tau^2}, \qquad \sigma_{\mathrm{T}} = \sigma_1 - \sigma_2 = \sqrt{\sigma^2 + 4\tau^2}, \tag{B4.1}$$

so that $1 \le \sigma_{\mathrm{T}}/\sigma_{\mathrm{vM}} \le 2/\sqrt{3}$, with the upper bound in pure torsion. Inserting $\sigma = 32K_bM/(\pi d^3)$ and $\tau = 16K_tT/(\pi d^3)$ gives (4.3) and its Tresca counterpart

$$d_{\mathrm{T}} = \Big[\frac{32}{\pi\sigma_{\mathrm{adm}}}\sqrt{(K_bM)^2 + (K_tT)^2}\Big]^{1/3}. \tag{B4.2}$$

For $\chi = 1$, Tresca gives 38.5 mm against the 37.2 mm of Table 4.1 (+3.5%). The diameter ratio can never exceed $(2/\sqrt{3})^{1/3} = 1.049$, so the choice of criterion matters far less than the torque fraction χ or the force arm.

Energy methods and shear deformation

For a stepped section with bending moment $M(x)$ and shear force $V(x)$, Castigliano's theorem gives the deflection under a unit dummy load as

$$\delta = \int_0^{\ell} \frac{M\,\bar{m}}{EI(x)}\,dx + \int_0^{\ell} \frac{V\,\bar{v}}{\kappa GA(x)}\,dx, \tag{B4.3}$$

which accumulates the segment compliances of the drawn steps. For a uniform overhang loaded at its end, $\bar{m} = x$ and $\bar{v} = 1$. With the Timoshenko shear coefficient of a solid circle, $\kappa = 6(1+\nu)/(7+6\nu) = 0.886$,

$$\delta = \frac{F\ell^3}{3EI} + \frac{F\ell}{\kappa GA}, \qquad \frac{\delta_s}{\delta_b} = \frac{3(1+\nu)\,d^2}{8\kappa\,\ell^2}. \tag{B4.4}$$

The 32.1 mm section with a 50 mm arm has $\ell/d = 1.56$, which gives $\delta_s/\delta_b = 0.227$. The deflection becomes $10.7 + 2.4 = 13.2\,\mu\mathrm{m}$, 23% above the Euler–Bernoulli value of Section 4.2. Bearing and support compliances add in series and must enter the same clearance budget.

Fatigue of a stationary axle

The axle does not rotate: the wheel turns on the bearing pair (Plate C.1). Bending is therefore not reversed once per revolution. Each landing roll applies, to first order, one cycle from zero to its maximum ($R = 0$). Bending and braking torque rise together, so the loading is proportional and the von Mises amplitude and mean are both $\sigma_{\max}/2$. The modified Goodman line $\sigma_a/S_e + \sigma_m/S_u = 1/n_f$ then admits

$$\sigma_{\max} \le \frac{2}{n_f\,(1/S_e + 1/S_u)}. \tag{B4.5}$$

The endurance limit is corrected with Marin factors, $S_e = k_a k_b k_c \cdots S'_e$, $S'_e \simeq 0.5\,S_u$, using $k_a = 4.51\,S_u^{-0.265}$ for a machined finish (S_u in MPa) and $k_b = 1.24\,d^{-0.107}$ for $2.79 \le d \le 51$ mm. For an illustrative steel with $S_u = 600$ MPa and $d = 32.1$ mm, $k_a = 0.828$, $k_b = 0.856$ and $S_e = 212$ MPa, so $\sigma_{\max} \le 157$ MPa at $n_f = 2$. The 108.9 MPa of Table 4.1 for $\chi = 1$ lies under this line, although it exceeds the 70 MPa static reference. The two checks answer different questions. A real material certificate and the notch factors $K_f = 1 + q(K_t - 1)$, with notch sensitivity $0 \le q \le 1$, replace the illustrative inputs. Using K_t in place of K_f, as in Table 4.1, errs on the safe side.

Finite life and load spectra

The number of cycles is set by landings, not revolutions. For a design life of N stops, a Basquin law $\sigma_a = \sigma'_f(2N)^b$ with the mean-stress correction $\sigma_{ar} = \sigma_a/(1 - \sigma_m/S_u)$ replaces the infinite-life line. Variable stop severities combine through Miner's rule, $\sum_j n_j/N_j \le 1$, as for the bearings in (3.7). Ground loads during taxiing and side loads add smaller, more numerous cycles, and their spectrum is part of the corner-load measurements of Table 7.2.

4.4 Clamped joints between rotor, hub and rim

Brake torque crosses more than one interface. The note records eight ISO 4017 M5 class 8.8 fasteners for the disc interface and identifies 5,329 N and 4.14 N·m. The parts list gives eight M6 × 25 for “Vis disque-liaison” and eight M6 × 16 for “Vis disque-jante”. The cap fasteners also differ between the text and parts list. For cap 1 the parts list and assembly sequence give quantities of three and one, respectively. The H–H annotation in Plate C.2 associates a nominal 5,329 N and 4.14 with the axle-nut/spacer assembly. Table 4.2 keeps these references visible as configuration items. The same numerical preload can be used as a sensitivity case for the rotor joint without assigning it to that hardware.

Table 4.2 – Fastener references that require a common drawing revision. Part identification follows Plate C.1.

Interface	Note and assembly sequence [1]	Parts list, Plate C.1
Disc and connection ring	Eight M5, grade 8.8	Eight M6 × 25 (item 15, “Vis disque-liaison”)
Rim-side connection	Eight M6	Eight M6 × 16 (item 12, “Vis disque-jante”)
Cap 1	Four M5	Four M6 × 25 (item 2)
Cap 2	Four M6	Four M6 × 12 (item 4)
Airframe-side and axle nuts	Two M18 nuts	Item 20 M18, item 6 diameter unspecified

For a fully clamped friction interface, an axisymmetric friction estimate integrates the contact pressure $p_c(r)$ over the active contact area.

$$T_{\mathrm{slip}} = \int_A \mu_j p_c(r) r \, \mathrm{d}A = \mu_j F_c r_{\mathrm{eff}}. \tag{4.7}$$

The effective radius is the pressure-weighted radius, and F_c is the resultant normal clamp force on that interface. With n fasteners initially loaded to F_0 and a retained fraction η_r,

$$F_c = n \eta_r F_0, \qquad \mu_{j,\min} = \frac{T_w}{n \eta_r F_0 r_{\mathrm{eff}}}. \tag{4.8}$$

At n=8, F_0=5,329 N, μ_j=0.12 and r_{eff}=47.5 mm, the ideal slip limit is 243.0 N·m. Values above μ_j=0.129 are needed for 260.7 N·m if preload is fully retained. With 85% retention the requirement rises to 0.151. The 47.5 mm effective radius illustrates the scale of a drawn Ø95 feature. The contact annulus and pressure distribution still require confirmation. Each connection in series sees the transmitted torque. Its effective radius, clamp, coefficient and number of friction faces are assessed individually.

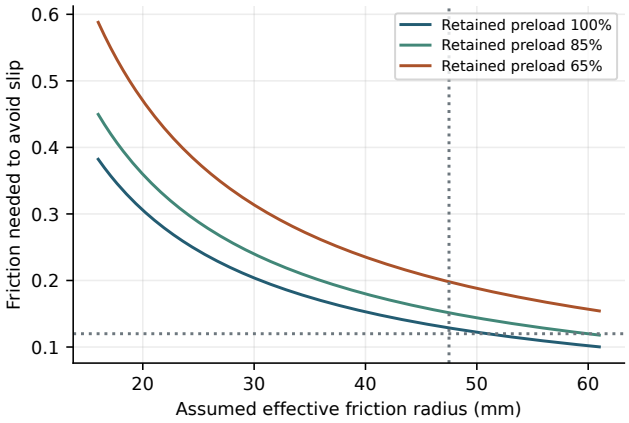

Figure 4.4 – Minimum interface friction to transmit 260.7 N·m without slip for eight fasteners at 5,329 N initial clamp each. Reference lines are drawn at 47.5 mm and μ_j=0.12. Declining retained clamp shifts the curve upwards.

If the joint slips and a bolt group is intended to carry direct tangential load, equal radius and equal load sharing give $F_{sh}=T_w/(n r_b)$, where r_b is bolt pitch radius. Taking 47.5 mm for r_b in a separate illustration gives 686 N per fastener. The pitch radius is measured from fastener positions, and the effective friction radius is obtained from the clamped contact. Clearance, bolt bending and unequal engagement can increase the maximum shank load.

A nominal bearing pressure at the side wall is $p_b=F_{sh}/(d_b\, t_p)$, with shank diameter d_b and plate

Box 4.2 Mechanics of the clamped rotor joint: torque–preload, stiffness and preload loss

Theoretical complement to Section 4.4. Values computed by brake_theory.py (Appendix D) for M5 class 8.8 at $F_0 = 5329$ N; the 10 mm grip and steel members are illustrative.

Torque–preload relation

The tightening torque is split between the thread, which lifts the bolt and works against thread friction, and the bearing face of the head or nut. In the rounded form used by VDI 2230,

$$T = F_0\Big[0.16P + 0.58\,d_2\,\mu_G + \frac{D_{Km}}{2}\,\mu_K\Big], \qquad \text{(B4.6)}$$

where P is the pitch, d_2 the pitch diameter, $D_{Km} = (d_w + d_h)/2$ the mean bearing diameter and μ_G, μ_K the thread and head friction coefficients. For M5 ($P = 0.8$ mm, $d_2 = 4.480$ mm, $D_{Km} = 6.75$ mm) at $\mu_G = \mu_K = 0.12$, 5329 N requires 4.50 N·m. The recorded 4.14 N·m corresponds to $\mu = 0.109$, which is equivalent to the nut factor $K_n = 0.155$ of Section 4.4. For M6 the same preload requires 5.49 N·m. The torque method transmits friction scatter into preload: at a fixed 4.14 N·m, μ between 0.08 and 0.16 gives 6.83 to 3.82 kN, that is +28% and −28% about the nominal value.

Stress during tightening

The shank carries the axial stress $\sigma = F_0/A_s$ and the torsion of the thread torque $M_G = F_0(0.16P + 0.58\,d_2\mu_G)$ on the section of diameter $d_s = (d_2 + d_3)/2$:

$$\sigma_{\mathrm{red}} = \sqrt{\Big(\frac{F_0}{A_s}\Big)^2 + 3\Big(\frac{16M_G}{\pi d_s^3}\Big)^2}. \qquad \text{(B4.7)}$$

For M5 this gives $\sigma = 375$ MPa, $\tau = 156$ MPa and $\sigma_{\mathrm{red}} = 462$ MPa, or 72% of $R_{p0.2} = 640$ MPa for class 8.8. The nominal preload thus leaves margin for torque scatter and thermal increments.

Joint diagram

Bolt and clamped members act as springs in series for preload and in parallel for an external axial load F_A. With a fully threaded grip l_k and the 30° pressure-cone model for two identical steel members,

$$k_b = \frac{EA_s}{l_k}, \quad k_m = \frac{0.5774\,\pi E d}{2\ln\dfrac{5(0.5774\,l_k + 0.5d)}{0.5774\,l_k + 2.5d}}, \quad \Phi = \frac{k_b}{k_b + k_m}. \qquad \text{(B4.8)}$$

The bolt force and the residual clamp then follow

$$F_S = F_0 + \Phi F_A, \qquad F_K = F_0 - (1-\Phi)F_A, \qquad \text{(B4.9)}$$

with separation at $F_A = F_0/(1-\Phi)$. For $l_k = 10$ mm, $k_b = 298$ kN/mm, $k_m = 1166$ kN/mm and $\Phi = 0.204$. Only a fifth of an external load reaches the bolt, and separation needs 6.69 kN.

Preload losses

Embedding of the roughness peaks under the head, in the thread and in the joint faces produces a permanent loss

$$\Delta F_Z = f_Z\,\frac{k_b k_m}{k_b + k_m}, \qquad f_Z \simeq 3.29\Big(\frac{l_k}{d}\Big)^{0.34}\ \mu\mathrm{m}. \qquad \text{(B4.10)}$$

Here $f_Z = 4.16$ µm gives $\Delta F_Z = 0.99$ kN, so 81.4% of the preload is retained, close to the 85% scenario of Fig. 4.4. With (4.8), the slip limit falls to 198 N·m at $\mu_j = 0.12$, and transmitting 260.7 N·m then needs $\mu_j \geq 0.158$.

Temperature acts through differential expansion. If the clamped parts run ΔT above the bolt,

$$\Delta F_T = \alpha\,\Delta T\,l_k\,\frac{k_b k_m}{k_b + k_m} = 28.5\ \mathrm{N/K} \times \Delta T. \qquad \text{(B4.11)}$$

A difference of 100 K changes the clamp by 53% of F_0. A rotor flange that heats before its fasteners raises the bolt load during the stop. The clamp then falls back as the temperatures equalise, while the elastic modulus and relaxation at temperature reduce it further. The friction-joint check (4.8) must therefore hold over the temperature histories of Section 6, not only at assembly.

Slip versus positive drive

The interface can carry T_w by friction while $T_w \leq n\eta_r F_0 \mu_j r_{\mathrm{eff}}$, with η_r the retained preload fraction. Beyond that limit, the bolts are loaded in shear and bearing as described in Section 4.4. A design that relies on friction needs η_r and μ_j as measured quantities; a positive drive (dowels, splines or fitted bolts) removes the dependence on them.

thickness t_p. Under a washer or fastener head, mean compressive pressure instead uses the seated annular area $A_h=\pi(D_h^2-D_o^2)/4$ and the clamp load. The 241 MPa in the note is therefore retained as a reported value which needs a defined loaded area and force before comparison to an allowable. The slip model and local contact pressure checks require different inputs.

A common torque–preload model is $T_{tight}=K_n\, d_b\, F_0$ [5]. If 4.14 N·m and 5,329 N were paired, the implied K_n would be 0.155 for M5, 0.129 for M6 and 0.043 for M18. The formula condenses thread and seating friction into a factor. Each size needs its own verified torque–preload relationship. Clamp-setting and bearing endplay use distinct verification methods. A physical joint also requires fastener proof, engaged thread length, local bearing and fatigue checks.

5. Floating caliper and friction track

5.1 Clamp force and available torque

The design selects a floating caliper with one piston, two pads and return springs [1]. In the ideal sliding case the piston applies $F_p=pA_p$ to one pad and the reaction through the moving body applies the same force to the other pad. With piston radius 13 mm, $A_p=530.93$ mm². At the note's 280 bar, $F_p=14.87$ kN, consistent with its rounded 15 kN. The two-pad normal-force sum in this ideal model is 29.73 kN.

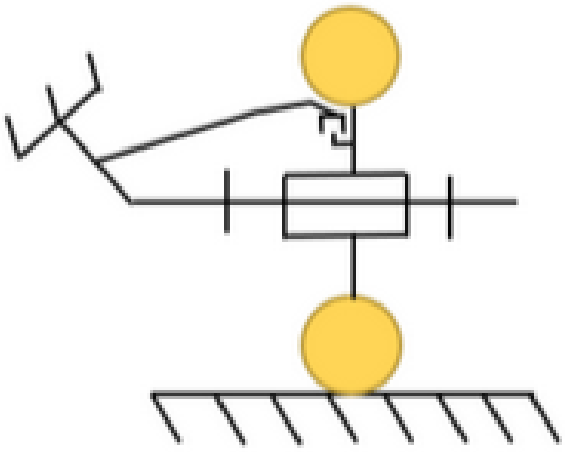

Figure 5.1 – Original floating-caliper functional sketch [1, p. 6].

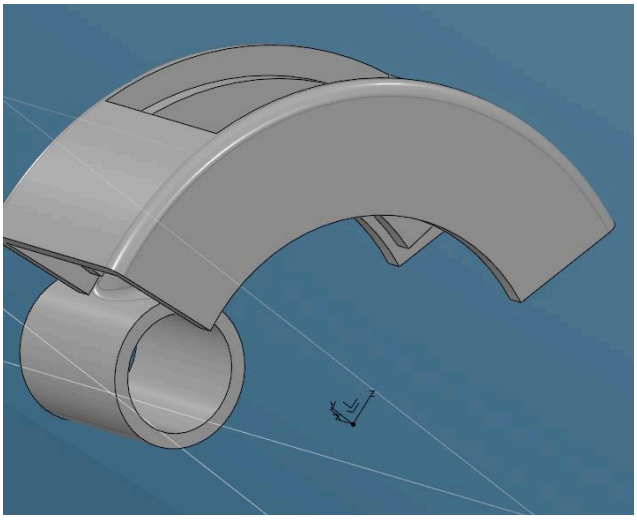

Figure 5.2 – Original CAD view of the piston and floating caliper concept [1, p. 13].

The torque per face is the moment of the tangential stress over the pad contact. For equal friction coefficients μ_p and effective radii r_f on both faces, the result is

$$A_p=\pi r_p^2, \qquad F_p=pA_p, \qquad T_w=2\mu_p F_p r_f. \tag{5.1}$$

This ignores sliding resistance and any return force that acts at the chosen application stroke. Those effects reduce the available force. A pressure margin also has to cover temperature-dependent coefficient, seal drag, supply losses and possible pressure differences between wheels.

5.2 Effective pad radius

For a pad sector of constant angular width and radial limits r_i,r_o, normal pressure q(r) over one face

determines the mean moment arm. The sector width cancels in the quotient of the two integrals.

$$r_f = \frac{\int_{r_i}^{r_o} q(r) r^2 \, \mathrm{d}r}{\int_{r_i}^{r_o} q(r) r \, \mathrm{d}r}. \tag{5.2}$$

For uniform pressure q is constant. For the ideal uniform-wear case, wear rate proportional to pressure times sliding speed is the same across the track, so q(r)r is constant at a fixed rotational speed. Integrating yields

$$r_{f,p} = \frac{2}{3}\frac{r_o^3 - r_i^3}{r_o^2 - r_i^2}, \qquad r_{f,w} = \frac{r_o + r_i}{2}. \tag{5.3}$$

The screening geometry in Fig. 1.1 sets r_i=0.60 D/2 and r_o=D/2−2.5 mm. The limits are assumptions chosen to isolate the diameter effect. At 125 mm the effective radius is 49.62 mm under uniform pressure and 48.75 mm under uniform wear. At 160 mm these become 63.91 and 62.75 mm. Differences from pressure distribution are small relative to the diameter effect within this geometry family. Pad taper, radial wear patterns and hot distortion alter that comparison.

5.3 Pressure envelope and hot friction

At a specified torque, smaller r_f raises the pressure needed for the same μ_p. Both pressure and available torque scale directly with the piston area. Inverting Eq. (5.1) gives

$$p_{\mathrm{req}} = \frac{T_w}{2\mu_p A_p r_f}, \qquad \mu_{p,\min} = \frac{T_w}{2 p_{\max} A_p r_f}. \tag{5.4}$$

Table 5.1 – Hydraulic demand at 260.7 N·m per wheel, equal pad loads and uniform wear.

Case	Effective radius (mm)	p at μ=0.30 (bar)	p at μ=0.15 (bar)
125 mm	48.75	168	336
160 mm	62.75	130	261

At 260.7 N·m and μ_p=0.30, the pressure is 168 bar for the capped disc and 130 bar for the drawn disc in the uniform-wear case. At μ_p=0.15, the 125 mm case rises to 336 bar. At 280 bar the respective friction thresholds are 0.180 and 0.140. They can be used as test acceptance inputs once the actual wheel torque and pad geometry are established. The two friction values are model scenarios and are independent of the runway coefficient in Section 2.

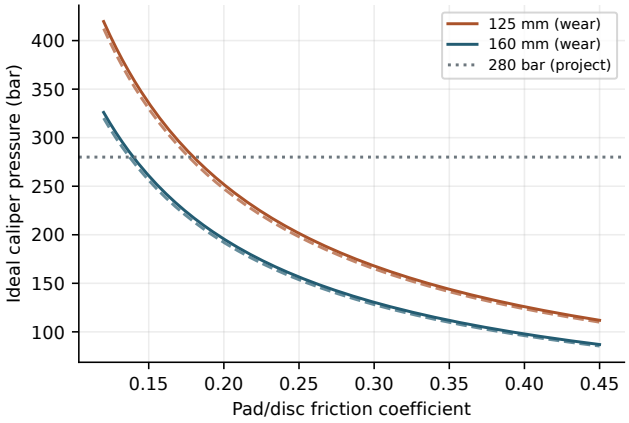

Figure 5.3 – Pressure needed for 260.7 N·m. Solid curves use the uniform-wear radius, dashed curves use uniform pressure. The horizontal line is the 280 bar value in the technical dossier.

A geometric feasibility check follows directly. At μ_p=0.15 and pressure 280 bar, the effective radius required for the reference torque is 58.5 mm. For the 125 mm model, r_o=60 mm. In the uniform-wear formula the inner track would need to lie near 57 mm, leaving only about 3 mm of radial width. The available pad area and heat flux at the contact would be problematic for that geometry. Holding the assumed radius and increasing piston diameter gives an ideal lower bound near 28.5 mm for this low-friction scenario. Clearance, stroke, allowable cylinder pressure and cooling still constrain any geometry change. A hot-friction measurement may make one or both alternatives unnecessary.

A coupled design formulation would use an experimentally determined $\mu_p(T_s,p,\omega)$ and enforce the torque requirement over the entire stop. Available torque can fall during a stop if track heating lowers friction while the demand remains high. The present models provide the two separate

Box 5.1 Pad contact, wear, hot friction and friction-induced dynamics

Theoretical complement to Sections 5.1–5.4. Values computed by brake_theory.py (Appendix D); the fade coefficient and the parameter ranges of the pressure study are illustrative.

Archard wear and the uniform-wear radius

Archard's law makes the local wear depth rate proportional to pressure and sliding speed, $\dot{w} = k_A\, p\, v_s$, with $v_s = \omega r$ and a specific wear rate k_A. A rigid backing plate on a flat rotor imposes the same axial wear everywhere after run-in, so $p(r)\, r$ must be constant:

$$p(r) = p_{\max}\frac{r_i}{r}, \qquad F_n = \theta_p\, p_{\max} r_i (r_o - r_i), \quad \text{(B5.1)}$$

for a pad sector of angle θ_p. The peak pressure sits at the inner edge, and the torque per face $\mu_p \theta_p p_{\max} r_i (r_o^2 - r_i^2)/2$ gives $r_{f,w} = (r_o + r_i)/2$ of (5.3). Comparing with the uniform-pressure radius,

$$r_{f,p} - r_{f,w} = \frac{(r_o - r_i)^2}{6\,(r_o + r_i)} \geq 0. \quad \text{(B5.2)}$$

The difference is 0.87 mm at 125 mm and 1.16 mm at 160 mm, as in Section 5.2. A new pad therefore loses about 1.8% of torque during bedding-in. Integrating Archard's law over a stop gives the worn volume

$$V = k_A \int F_n v_s\, dt = \frac{k_A\, W_f}{\mu_p}, \quad \text{(B5.3)}$$

where W_f is the friction work of the pad pair. At 551.3 kJ and $\mu_p = 0.30$, the sliding work $W_f/\mu_p = 1.84$ MN·m per stop fixes pad life once k_A is measured.

Hot friction and fade

Let the pad coefficient fall with track temperature as $\mu_p = \mu_0/[1 + \kappa_f(T_s - T_0)]$. Holding the demanded torque then requires

$$p(t) = p_0\,[1 + \kappa_f\,(T_s(t) - T_0)]. \quad \text{(B5.4)}$$

With an illustrative $\kappa_f = 5 \times 10^{-4}\,\mathrm{K}^{-1}$ and the track peaks of Table 6.2, the factors are 1.18 and 1.28. Starting from 130 and 168 bar at $\mu_0 = 0.30$, this gives 154 bar for the drawn rotor and 215 bar for the comparable-relief 125 mm rotor, both below 280 bar. At fixed pressure the torque falls by the same factors instead. This loop between temperature, friction and torque is the coupled formulation of Section 5.3.

Floating-caliper efficiency and hydraulics

Guide-pin friction $F_g = \mu_g N_g$ reduces the force reaching the outer pad. The available torque becomes

$$T_w = \mu_p\,(2F_p - F_g)\,r_f, \qquad \eta_c = 1 - \frac{F_g}{2F_p}. \quad \text{(B5.5)}$$

The line pressure obeys a compliance balance, $C_h \dot{p} = Q - \sum_i A_{p,i}\dot{x}_{p,i}$, with $C_h = V/K_{\mathrm{fl}} + \sum \partial V/\partial p$ for fluid bulk modulus K_{fl} and hose expansion. With a supply restriction $Q = (p_s - p)/R_h$ the response is first order with $\tau_h = R_h C_h$. Through (5.5) and τ_h, hose and seal compliance set pedal travel and application delay.

Mode coupling and squeal

In a two-degree-of-freedom model, the normal pad displacement x_1 and a tangential rotor mode x_2 (equal modal masses m) are coupled by the friction force $\mu k_c x_1$:

$$m\ddot{\boldsymbol{x}} + \begin{bmatrix} k_1 & k_3 \\ k_3 + \mu k_c & k_2 \end{bmatrix} \boldsymbol{x} = \boldsymbol{0}. \quad \text{(B5.6)}$$

The non-symmetric stiffness matrix has eigenvalues

$$m\omega^2 = \tfrac{1}{2}\Big[k_1 + k_2 \pm \sqrt{(k_1 - k_2)^2 + 4k_3(k_3 + \mu k_c)}\Big]. \quad \text{(B5.7)}$$

They become complex, giving a growing oscillation, once

$$\mu > \mu_c = \frac{k_3 + (k_1 - k_2)^2/(4k_3)}{-k_c}, \qquad k_3 > 0 > k_c. \quad \text{(B5.8)}$$

Close modal frequencies ($k_1 \simeq k_2$) lower μ_c. This mode-coupling mechanism of squeal needs no negative friction slope, and modal tests of the caliper on its bracket provide its parameters.

Pressure demand under uncertainty

With $\mu_p \sim \mathcal{U}(0.25, 0.40)$, $R \sim \mathcal{U}(150, 166)$ mm and brake share $\lambda \sim \mathcal{U}(0.50, 0.60)$ in $T_w = \lambda F_b R$, 2×10^4 samples of (5.4) give a median, 95th percentile and maximum of 162, 209 and 239 bar at 125 mm, and 126, 162 and 186 bar at 160 mm. None exceeds 280 bar; the margin is consumed only below the thresholds 0.180 and 0.140 of Section 5.3.

curves needed to construct that coupling after data are available.

5.4 Actuation and return

The source separates the caliper geometry from full hydraulic sizing. The circuit concept contains a pedal, a master stage, downstream hydraulic stages connected to the calipers, fluid reservoirs and a maintenance unit. With an ideal pedal mechanical advantage i_p and master area A_m, an ideal pressure rise is $p=i_pF_{ped}/A_m$. Stroke and volume must cover the pad gaps for both brakes and system compliance. At a first approximation,

$$A_m\Delta x_m=\sum_i A_{p,i}\Delta x_{p,i}+C_h\Delta p. \tag{5.5}$$

The return springs provide preload or retraction over the release displacement. A linear spring gives $F_s=k_s\Delta x_s$. Spring choice depends on actual seal rollback, sliding friction and release clearance. The nominal application force of 14.87 kN is a force for torque generation. The return spring is assessed from the unloaded and partially released force balance. Pressure modulation, temperature at the fluid and pad wear deserve separate bench measurements.

6. Thermal modelling and design sizing

6.1 Rotor mass and energy scale

The project note records a 2.791 kg disc and a temperature comparison from 25 °C to 450 °C. It also records 530 kJ as absorbed energy, 470 kJ as dissipated energy and a 38 s cooling estimate [1, p. 12]. The stated $mv_0^2/2$ calculation gives 3.92 kJ with the disc mass, or 962.1 kJ with the aircraft mass. The aircraft and the moving wheels determine the mechanical work. The disc mass determines its heat capacity. Sections 2 and 6 use 551.3 kJ of mechanical work per ideal wheel at the reference point and partition that work explicitly.

Let D be the external diameter, D_i=32.10 mm the bore, b=22 mm the thickness and ρ=7,850 kg/m³ the assumed density. A solid annulus has mass and geometric exchange-area proxy

$$\begin{aligned} M_{\text{ann}}&=\frac{\rho\pi b}{4}(D^2-D_i^2),\\ A&=\frac{\pi}{2}(D^2-D_i^2)+\pi b(D+D_i). \end{aligned} \tag{6.1}$$

The area includes both planar faces, outer periphery and bore. It omits pad shielding, hole walls, reliefs and the air path in the assembly. Varying h at fixed reference area probes the effect of changing the product hA. At 160 mm the solid-annulus mass is 3.333 kg and A=0.0519 m². The reported mass implies a retained solid fraction f_m=2.791/3.333=0.8375. At 125 mm the same approximation gives 1.658 kg at that fraction, or 1.980 kg as a solid bound, with A=0.0338 m² in both cases.

The notebook calculation counts 160 hole-wall contributions and 18 lateral reliefs. Plate C.3 specifies Ø3.00 × 80 for small holes and Ø6.00 × 8 at the centre. Even if all these labelled cylinders traversed the full 22 mm, they would remove about 0.137 kg in the density model, from $\Delta M=\rho\pi\, b\sum_j n_j d_j^2/4$. The difference between 3.333 kg and the reported 2.791 kg is about 0.542 kg. The full mass reconciliation would also require the stepped centre, geometry of reliefs and through-depth information. For cooling, the wetted part of each internal surface and its local flow are needed. Effective exchange area depends on both the wetted surfaces and their local flow.

Define β as the effective heat fraction entering the rotor at the friction interface. A constant partition is a modelling assumption for this event. A perfectly insulated and spatially uniform disc then gives

$$T_{\text{ad}}=T_0+\frac{\beta W_{b,w}}{M_d c_p}. \tag{6.2}$$

Table 6.1 – Thermal inputs assigned for the screening model. Values in brackets are sensitivity cases.

Input	Reference	Basis
Density	7,850 kg/m³	Generic steel proxy
Specific heat	500 J/(kg·K)	Held constant
Ambient and initial	25 °C [+50, +95 K]	Ambient fixed
Rotor heat share	0.80 [0.60–0.95]	Boundary scenario
Initial convection	200 [50–400] W/(m²·K)	Boundary scenario
Stopped convection	20 W/(m²·K)	Boundary scenario
Emissivity	0.70	Boundary scenario
Track/node thermal coupling	90 [45–180] W/K	Model sensitivity
Track share, capacity / area	0.50 / 0.65	Lumped geometry

At β=0.80, the rotor receives 441.0 kJ and the adiabatic mass requirement to stay at or below 450 °C from a cold 25 °C start is 2.075 kg. This conservative mass target concerns bulk temperature in the one-node model and neglects external cooling. In the 22 mm family, even the capped solid mass is below this adiabatic mass. Its adiabatic bulk temperature is 471 °C. Within the comparable-relief model the same target corresponds to roughly 27.5 mm of thickness before cooling. Heat partition, actual heat capacity and local track gradients remain design variables.

6.2 Spatially averaged transient temperature

The lumped energy equation uses thermal inertia and time-dependent heat rejection [6]. Define T_a as the constant ambient temperature and use subscript k for absolute temperature in kelvin. Treat the cooling surroundings as large and at T_a. The balance is

$$M_d c_p \frac{\mathrm{d}T}{\mathrm{d}t} = \beta P_w - \dot{Q}_{\mathrm{conv}} - \dot{Q}_{\mathrm{rad}}, \tag{6.3}$$

$$\dot{Q}_{\mathrm{conv}} = h(t)A(T - T_a), \qquad \dot{Q}_{\mathrm{rad}} = \varepsilon\sigma_{\mathrm{SB}}A(T_k^4 - T_{a,k}^4). \tag{6.4}$$

During braking the model uses $h_0+(h_v-h_0)(v/v_0)^{0.8}$, with reference coefficients h_0=20 W/(m²·K) and h_v=200 W/(m²·K). After the stop it holds the baseline h_0 and sets P_w=0. The assumed speed law represents declining forced convection during deceleration. Taking h_v=400 in the sweep reproduces the scale of the original upper convection input at application. The powers in Eq. (6.4) must be integrated over the temperature history. Evaluating convection at the limiting temperature for the whole event would apply the peak driving temperature even at the beginning of a cold stop. The original 38 s estimate corresponds to rejecting 470 kJ at about 12.4 kW throughout. In the model, heat rejection rises from zero at a cold start and declines during cooldown.

With c_p=500 J/(kg·K) the lumped storage term changes linearly with average temperature. A Biot estimate uses L_c=V/A and Bi=h L_c/k_s. For the 125 mm solid-envelope geometry, L_c≃7.5 mm. With k_s=40 W/(m·K) as an illustrative conductivity, Bi≃0.038 at h=200 W/(m²·K). That scale supports a bulk external-cooling approximation in an evenly heated solid. The actual pad input is local, and radial and thickness gradients remain possible even at a small external Biot number. The next model treats one internal temperature difference explicitly.

A typical prescribed steel expansion coefficient 12×10^{-6} K^{-1} over a spatially uniform 425 K rise produces about 0.32 mm of radial expansion at radius 62.5 mm and about 0.11 mm through 22 mm thickness. This yields a dimensional scale to compare against clearances. Real pad gap change also depends on temperature gradients, restraint, elastic deformation and caliper/support expansion.

6.3 Track and core temperatures

The two-node network assigns all external heat input to a friction-track node and uses an internal conductance G_{sc} to the remainder of the rotor. The heat capacity split is C_s=C_c=$M_d c_p$/2. The external area split is A_s=0.65A, A_c=0.35A. These partitions specify the reference scenario. For each node i, let $L_i(T_i,t)$ denote its convective plus radiative loss with its own area. Then

Box 6.1 Heat partition, surface temperature and thermal stress in the friction track

Theoretical complement to Sections 6.1–6.3. Values computed by brake_theory.py (Appendix D) with the steel proxy of Table 6.1 (k_s = 40 W/(m·K)) and the track radii of Fig. 1.1; pad properties are illustrative.

Partition between rotor and pad

For two semi-infinite bodies sharing the flux $q = q_d + q_p$ and a common surface temperature, each surface rises as $2q_i\sqrt{t}/(e_i\sqrt{\pi})$, so $q_d/q_p = e_d/e_p$:

$$\beta = \frac{e_d}{e_d + e_p}, \qquad e_i = \sqrt{k_i \rho_i c_i}. \tag{B6.1}$$

For the steel proxy, $e_d = 12.5 \times 10^3$ W s$^{1/2}$/(m^{2}K). An organic pad ($k = 1$, $\rho = 2500$, $c = 1000$) gives $\beta = 0.888$ and a sintered pad ($k = 20$, $\rho = 5000$, $c = 500$) gives $\beta = 0.639$, bracketing the reference 0.80. Pad coverage, contact resistance and the transfer layer are ignored, so β remains an identification target (Box 6.3).

Circumferential averaging

At $\omega_0 = 319$ rad/s (19.7 ms per turn) heat diffuses only $\sqrt{\alpha\, 2\pi/\omega_0} = 0.45$ mm per revolution. Below this depth the track sees the averaged flux

$$q(t) = \frac{\beta P_w(t)}{2A_f}, \qquad A_f = \pi(r_o^2 - r_i^2), \tag{B6.2}$$

2.86 MW/m^2 at 160 mm and 4.83 MW/m^2 at 125 mm at application. The Blok–Jaeger flash temperature stays in the outer fraction of a millimetre.

Duhamel solution and its validity

For a semi-infinite solid under a variable flux, superposition of impulse responses gives

$$T_s(t) - T_0 = \frac{1}{e\sqrt{\pi}} \int_0^t \frac{q(\tau)}{\sqrt{t-\tau}}\, d\tau. \tag{B6.3}$$

For the linear flux $q_0(1 - t/t_s)$ of the reference stop,

$$T_s - T_0 = \frac{2q_0}{e}\sqrt{\frac{t}{\pi}}\Big(1 - \frac{2t}{3t_s}\Big), \tag{B6.4}$$

with a maximum $\frac{4}{3}(q_0/e)\sqrt{t_s/(2\pi)}$ at $t = t_s/2$. It holds only while $\alpha t/(b/2)^2 \lesssim 0.25$, i.e. $t \lesssim 3.0$ s; the 22 mm rotor is fully penetrated well before $t_s/2$.

Through-thickness transient

The finite track obeys

$$\partial_t T = \alpha\, \partial_{zz} T, \quad -k\, \partial_z T\big|_0 = q(t), \quad \partial_z T\big|_{b/2} = 0, \tag{B6.5}$$

solved by Crank–Nicolson on 111 nodes. Drilled holes parallel to z are homogenised by scaling k and ρc with the solid fraction, which leaves α unchanged. The scheme reproduces the constant-flux solution $2q\sqrt{t/\pi}/e$ to 9×10^{-6} and (B6.4) at 1 s to 0.02 K (292.2 K at 160 mm).

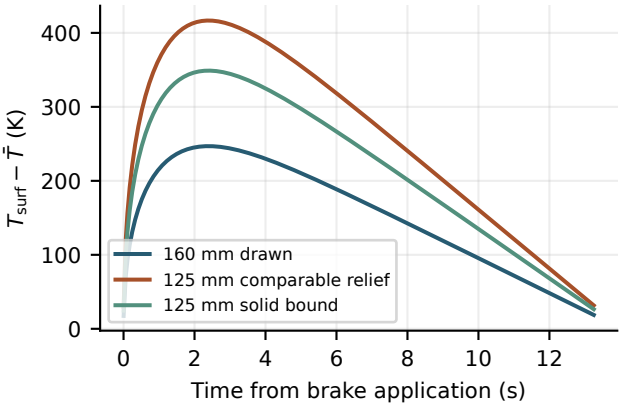

Surface minus mean track temperature from (B6.5).

The surface leads the mean by up to 247 K at 160 mm, 417 K at 125 mm with comparable relief and 349 K for the solid 125 mm bound, each about 2.4 s after application. It falls to 19–32 K by the stop: an early-stop gradient set by q_0/e.

Thermoelastic consequence

For a free plate heated symmetrically, compatibility removes the uniform and linear parts of $T(z)$ and leaves the in-plane stress

$$\sigma(z) = -\frac{E\alpha}{1-\nu}\,(T(z) - \bar{T}), \tag{B6.6}$$

with $E\alpha/(1-\nu) = 3.6$ MPa/K. At the peaks above, the elastic surface stresses are −889, −1500 and −1256 MPa. They exceed the hot yield strength of common steels: the skin yields in compression early in each heavy stop and is left in tension after cooling, the classical mechanism of heat checking and low-cycle thermal fatigue. These elastic upper bounds place hot strength and thermal fatigue of the track material in the bench programme of Table 7.2.

$$C_s \dot{T}_s = \beta P_w - G_{sc}(T_s - T_c) - \mathcal{L}_s(T_s, t), \tag{6.5}$$

$$C_c \dot{T}_c = G_{sc}(T_s - T_c) - \mathcal{L}_c(T_c, t). \tag{6.6}$$

Adding the equations cancels internal conduction and recovers the total storage balance. With equal capacity and negligible external loss, the temperature difference decays without input at rate $G_{sc}(1/C_s+1/C_c)$. At G_{sc}=90 W/K the corresponding equalisation time $M_d c_p/(4G_{sc})$ is about 3.9 s at 160 mm and 2.3 s at 125 mm with comparable relief. These are internal model timescales, shorter than the 13.25 s stop but long enough to produce appreciable track–core separation when the power is high.

The nodes represent spatial groups. The track temperature represents a surface zone. Flash temperatures, gradients around holes, asymmetry and thermal stress require finer spatial resolution. An identified thermal network or a spatial model can use test temperatures at multiple radii and depths. Published finite-element work on larger aircraft brakes illustrates the type of model-to-dynamometer comparison possible with a hardware programme [7]. The material and boundary inputs for the present steel proxy are listed in Table 6.1.

6.4 Reference temperatures and sensitivity

Table 6.2 – Temperature comparison for the same 13.25 s stop. Adiabatic and bulk columns are spatial averages. The track-node peak depends on the assumed internal conductance.

Design	Mass (kg)	Adiabatic (°C)	Bulk peak (°C)	Track peak (°C)	Track >450 °C (s)
160 mm drawn	2.791	341.0	329.7	390.3	—
125 mm, comparable relief	1.658	557.0	534.1	578.7	4.75
125 mm, solid bound	1.980	470.6	455.0	506.3	6.30

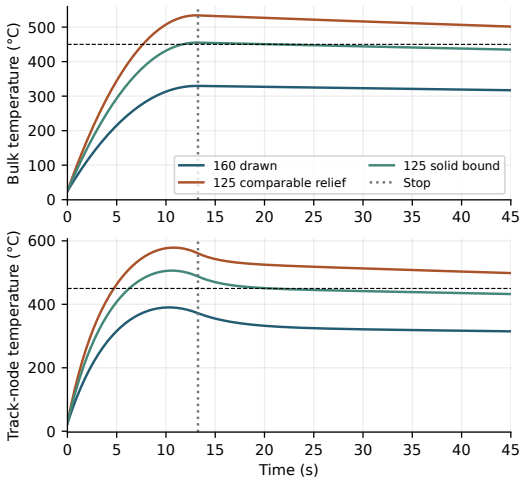

Figure 6.1 – Cold-stop temperature histories at the reference inputs. The upper panel is the one-node bulk solution, the lower panel the track in the two-node network. Vertical line at 13.25 s, horizontal line at 450 °C.

The 160 mm model reaches 329.7 °C as a bulk peak and 390.3 °C at the track node. The 125 mm comparable-relief case reaches 534.1 °C and 578.7 °C, respectively, with the track first exceeding the 450 °C line at the sampled time 4.75 s. The solid capped envelope increases mass by 0.322 kg and delays that crossing to 6.30 s in the same two-node family. Its peak is still 506.3 °C at the track and 455.0 °C in the bulk model. This ordering follows from the reduction in storage capacity as diameter falls. The lumped peak occurs slightly before the stop when cooling temporarily overtakes the remaining input. In the track model conduction to the cooler core also contributes to the earlier decline.

Table 6.3 – Heat rejected to ambient during braking in the one-node calculation.

Design	Conv. (kJ)	Rad. (kJ)
160 mm drawn	14.0	1.9
125 mm, comparable relief	15.3	3.8
125 mm, solid bound	12.9	2.5

The calculated one-node losses by the stop are only 15.9, 19.1 and 15.4 kJ for the three cases, compared with 441.0 kJ entering the rotor. Higher temperature in the lighter disc increases instantaneous losses, but also accompanies a substantially larger temperature rise for the same stored energy. In the 125 mm solid comparison, the

Box 6.2 Spectral structure of the thermal network, convection correlations and radiation

Theoretical complement to Sections 6.2–6.4. Closed forms checked against direct integration in brake_theory.py (Appendix D); air properties at a 450 K film temperature.

Mean and difference modes

Write the network (6.5)–(6.6) in terms of the capacity-weighted mean $\Sigma = (C_s T_s + C_c T_c)/(C_s + C_c)$ and the difference $\Delta = T_s - T_c$. Without external loss,

$$(C_s + C_c)\,\dot{\Sigma} = \beta P_w, \qquad \dot{\Delta} + \frac{\Delta}{\tau_1} = \frac{\beta P_w}{C_s}, \qquad \tau_1 = \frac{C_s C_c}{G_{sc}(C_s + C_c)}. \tag{B6.7}$$

Internal conduction thus leaves the mean untouched and relaxes only the difference. For the equal split of Section 6.3, $\tau_1 = M_d c_p/(4G_{sc})$. With the linear power $P_w = P_0(1 - t/t_s)$,

$$\Delta(t) = \frac{\beta P_0}{2G_{sc}}\Big[\Big(1 + \frac{\tau_1}{t_s}\Big)(1 - e^{-t/\tau_1}) - \frac{t}{t_s}\Big], \tag{B6.8}$$

which peaks at $t^* = \tau_1 \ln(1 + t_s/\tau_1)$ with

$$\Delta_{\max} = \frac{\beta P_0}{2G_{sc}}\Big(1 - \frac{t^*}{t_s}\Big). \tag{B6.9}$$

Rotor	τ_1 (s)	t^* (s)	$\Delta_{\max}$ (K)	with loss
160 drawn	3.88	5.76	209.1	204.4
125 relief	2.30	4.40	247.1	242.3
125 solid	2.75	4.84	234.7	230.5

Direct integration without loss reproduces (B6.9) to 2×10^{-5} K; external exchange lowers it by 4–5 K. The slow mode decays with $\tau_2 = C/[(h_0 + h_r)A]$: 769, 701 and 837 s at $h_0 + h_r = 35$ W/(m^{2}K). With $\tau_2/\tau_1 \approx 200$–$300$ the mean follows the one-node model (6.3) while $T_s \simeq \Sigma + \Delta/2$ adds a fast transient, hence the offset between the bulk and track columns of Table 6.2.

A physical estimate of G_{sc}

Taking the track node as the outer quarter-layers of the swept annulus and the core as its inner half, heat crosses $b/4$ through both faces:

$$G_{sc} \simeq \frac{2A_f\, f_m k_s}{b/4} = \frac{8 f_m k_s A_f}{b}. \tag{B6.10}$$

This gives 142 W/K (160 mm), 84 W/K (125 mm, comparable relief) and 100 W/K (125 mm, solid). These lie inside the 45–180 W/K sweep of Table 6.5 and scale with $A_f \propto D^2$, so G_{sc} is better not held fixed between diameters.

Forced convection

With $\nu = 32.4 \times 10^{-6}$ m^2/s, $k = 0.0373$ W/(m·K) and $Pr = 0.686$ [6], three classical limits bound h. For a free rotating disc in laminar flow ($Re_\omega = \omega r_o^2/\nu < 2.4 \times 10^5$),

$$Nu = \frac{h r_o}{k} = 0.36\, Re_\omega^{1/2} \;\Rightarrow\; h = 0.36\, k \sqrt{\omega/\nu}, \tag{B6.11}$$

which does not depend on radius: 42 W/(m^{2}K) at ω_0. For flow along the face with plate length D, the laminar and turbulent averages are

$$Nu_D = 0.664\, Re_D^{1/2} Pr^{1/3}, \qquad Nu_D = 0.037\, Re_D^{0.8} Pr^{1/3}, \tag{B6.12}$$

which give 70 and 164 W/(m^{2}K) at 160 mm (79 and 173 at 125 mm) at 53 m/s.

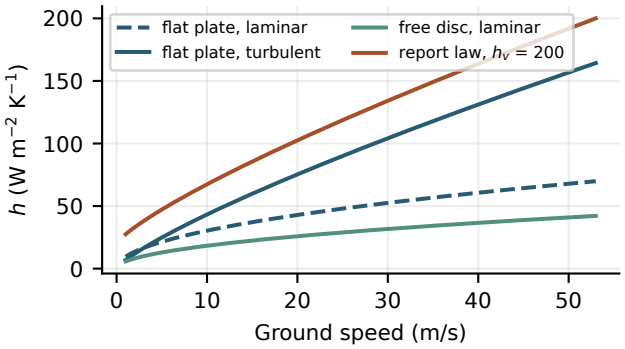

Classical limits and the convection law used in Section 6.

The exponent 0.8 of the report's law is the turbulent one, and $h_v = 200$ lies at the top of these estimates. The 50–400 sweep covers both regimes. Averaged over the stop, $(1 - t/t_s)^n$ weighs the forced part by $1/(1 + n)$: 0.556 for $n = 0.8$ against 0.667 for a laminar $n = 0.5$.

Radiation

Linearising $\varepsilon\sigma_{SB}(T_k^4 - T_{a,k}^4) = h_r(T - T_a)$ gives

$$h_r = \varepsilon\sigma_{SB}\,(T_k^2 + T_{a,k}^2)(T_k + T_{a,k}), \tag{B6.13}$$

that is 14.4 W/(m^{2}K) at 300 °C and 24.8 at 450 °C. Minor during braking (Table 6.3), it rivals h_0 in cooldown and governs recovery between stops (Box 6.3).

450 °C storage capacity is about 420.7 kJ. Thus, for this heat share it would need to reject about 20.3 kJ to stay at 450 °C at the end of the stop. The base model rejects 15.4 kJ, consistent with its bulk result just above that temperature.

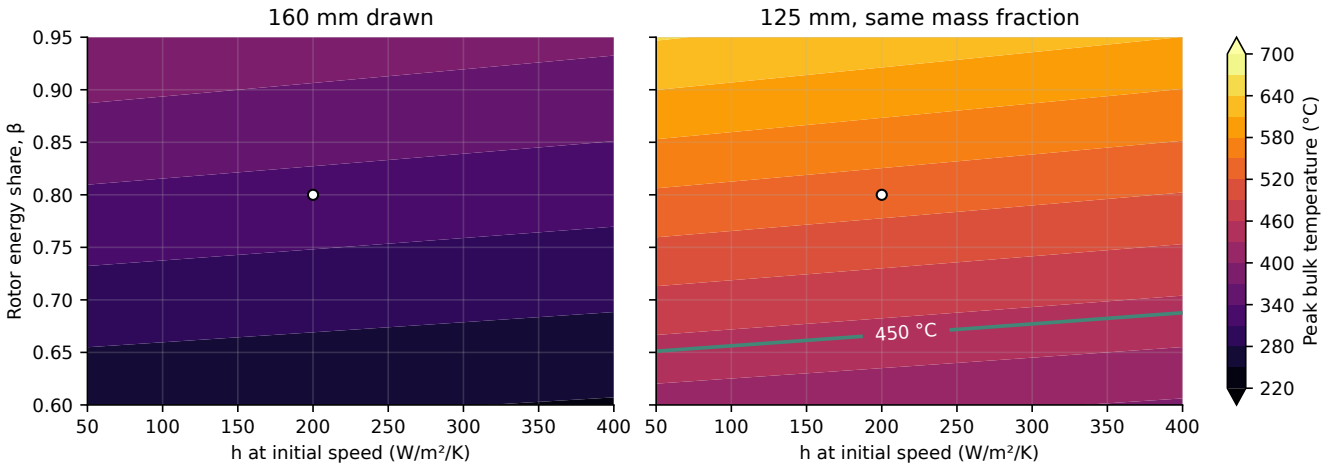

Figure 6.2 – Peak bulk temperature as a function of initial forced-convection coefficient and rotor heat share. White markers give the reference. The contour for 450 °C appears where the grid crosses that value.

Varying initial h from 50 to 400 W/(m²·K) and β from 0.60 to 0.95 produces 247–394 °C for the 160 mm bulk model and 396–642 °C for the comparable-relief capped bulk model. The ranges are extrema on the assumed grid. The 125 mm case crosses 450 °C within that grid as the share of energy retained by the rotor increases. Over the reference timescale, cooling affects the rise but heat capacity and partition dominate. A warm start increases all three bulk peaks (Table 6.4). The slower heat paths after the stop also affect recovery. In the one-node model at the base ambient and h_0, the 160 mm disc is around 292 °C and the comparable-relief 125 mm case around 444 °C at 100 s after stopping. These recovery projections hold the stopped-convection coefficient fixed.

Table 6.4 – Effect of initial rotor temperature. Ambient stays at 25 °C. Entries are peak bulk temperatures (°C).

Design	25 °C	75 °C	120 °C
160 mm drawn	329.7	376.2	418.0
125 mm, comparable relief	534.1	579.6	620.4
125 mm, solid bound	455.0	501.5	543.2

Table 6.5 – Effect of track-to-core conductance. Entries are peak track-node temperatures (°C).

G (W/K)	160 draw.	125 relief	125 solid
45	451.8	658.3	582.5
90	390.3	578.7	506.3
180	349.1	545.7	468.9

The trend in the two-node model depends on internal heat spreading. Reducing G_{sc} from 90 to 45 W/K moves the 160 mm track peak from 390 to 452 °C while its independent one-node prediction remains 330 °C. Increasing G_{sc} to 180 W/K moves that track peak to 349 °C. All capped cases in Table 6.5 exceed 450 °C at the track for the assigned β. The 450 °C line is the archived comparison temperature. A component temperature limit would require hot friction, material properties, fluid, seal and interface evidence.

6.5 Deceleration and inverse sizing

Figure 6.3 holds the same initial speed, constant residual thrust and reference thermal coefficients while changing the constant deceleration. At 1.2 m/s² the brake work increases to about 715 kJ per wheel and the reference-family stop lasts 44.2 s. The extra work dominates the additional convection time. For comparable relief the peak bulk temperature rises from 534 °C at 4.0 m/s² to 618 °C

at 1.2 m/s². A different thrust schedule or aerodynamic force history can change this dependence. The result is specific to the simplified longitudinal model and is separate from the adhesion constraint.

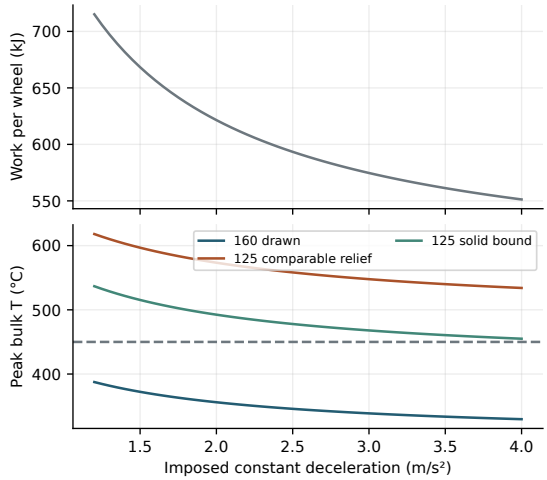

Figure 6.3 – Influence of deceleration on work and peak bulk temperature for constant 400 N thrust. All curves use the same thermal assumptions.

For the 125 mm case with comparable relief, solve for the thickness b at which the peak temperature equals 450 °C. The calculation keeps friction diameter, bore, solid fraction, c_p, G_{sc} and the heat share fixed, updates the mass and area from Eq. (6.1), and evaluates the two separate temperature models. A corresponding inverse calculation at fixed 22 mm solves for the largest model heat share at that threshold. Thickness changes outside geometry packaging have to be confirmed by a CAD revision. The inverse problem quantifies how much the thermal inputs would have to change.

Table 6.6 – Inverse sizing of the 125 mm envelope at 450 °C. The thickness solution holds β = 0.80. The heat-share solution holds thickness at 22 mm.

Start	Thermal state	Thickness (mm)	Mass (kg)	Heat share β
25 °C	Bulk	26.5	2.00	0.667
25 °C	Track	30.7	2.31	0.612
75 °C	Bulk	29.9	2.25	0.594
75 °C	Track	35.8	2.70	0.545

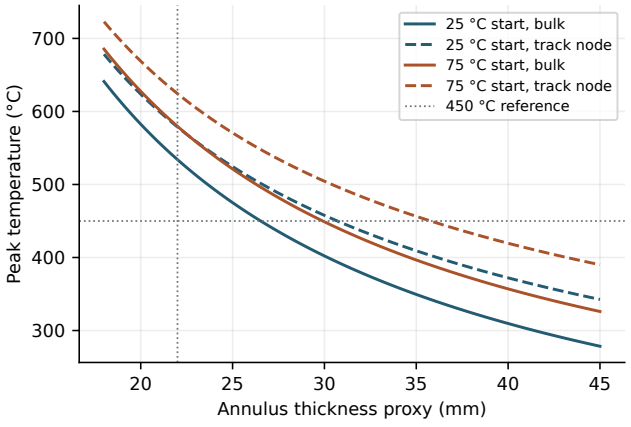

Figure 6.4 – Annulus thickness sensitivity for the 125 mm, comparable-relief model. Solid lines denote bulk temperature and dashed lines the track result. Vertical line marks the archived 22 mm height.

From a cold start the bulk model reaches the reference at 26.5 mm, about 2.00 kg. The track model under the same G_{sc} reaches it at 30.7 mm and about 2.31 kg, over 8 mm beyond the original 22 mm thickness. A 75 °C start shifts the latter result to 35.8 mm. Holding 22 mm instead, the cold track calculation requires β of about 0.612 or less, against the 0.80 input. Diverting that additional energy from the rotor would heat other components or change the event itself. It only helps if the heat receivers, component limits and torque output are all addressed. Revising thickness in CAD also calls for revisiting the internal conductance held fixed in this calculation.

Box 6.3 Repeated stops, inverse sizing as an implicit problem and parameter identifiability

Theoretical complement to Sections 6.4–6.6 and 7.2. Values computed by brake_theory.py (Appendix D) with the one- and two-node models of Section 6; the 600 s turnaround is an illustrative duty.

Stop-to-stop map and its fixed point

Let Φ map the rotor temperature at the start of a stop to the temperature at the start of the next one, after a turnaround Δt at h_0. A duty of identical stops is the iteration $T_{k+1} = \Phi(T_k)$. If $|\Phi'| < 1$ on an invariant interval, the contraction mapping theorem gives a unique attracting fixed point $T^* = \Phi(T^*)$. For linear losses retaining a fraction r of the excess per cycle, $u_{k+1} = r\,(u_k + \Delta T_{\text{stop}})$, and the geometric series gives

$$u^* = \frac{r\,\Delta T_{\text{stop}}}{1 - r}. \tag{B6.14}$$

Radiation makes r fall as temperature rises, so the nonlinear model is integrated directly.

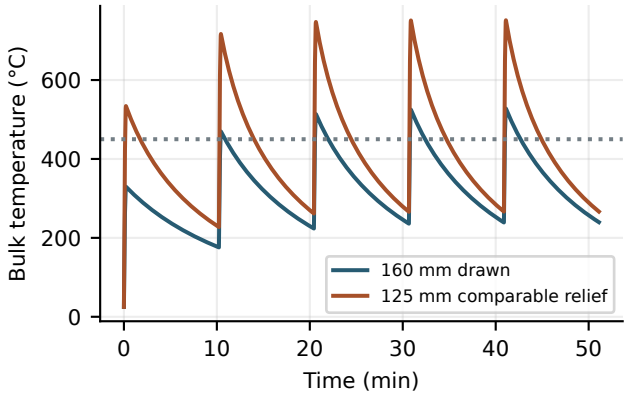

Bulk temperature over five reference stops 600 s apart (one-node model, cold first stop).

For the drawn rotor the bulk peaks are 329.7, 469.6, 513.7, 525.0 and 527.7 °C. Aitken extrapolation of eight stops gives a cyclic limit of 528.6 °C, reached from a start temperature of 239.9 °C, with $\Phi'(T^*) = 0.236$. The comparable-relief 125 mm rotor goes from 534.1 to 716.7 °C at the second stop and settles at 751.6 °C ($\Phi' = 0.120$). Under this duty even the drawn rotor exceeds the 450 °C comparison from the second stop, which is why Section 7.2 places repeated stops after the single-stop checks.

Inverse sizing and implicit sensitivities

The inverse problem of Section 6.5 solves $g(b, \boldsymbol{\theta}) = \max_t T(t; b, \boldsymbol{\theta}) - T_{\text{lim}} = 0$ for the thickness b at given parameters $\boldsymbol{\theta}$. Where $\partial g/\partial b \neq 0$, the implicit function theorem gives

$$\frac{\partial b^*}{\partial \theta_j} = -\frac{\partial g/\partial \theta_j}{\partial g/\partial b}. \tag{B6.15}$$

An independent implementation of the one-node model returns $b^* = 26.53$ mm and 2.00 kg for the cold bulk case, as in Table 6.6, with $\partial g/\partial b = -15.5$ K/mm. The sensitivities are +0.34 mm per 0.01 of β, −0.38 mm per 100 W/(m^{2}K) of h_v and +0.060 mm per kelvin of initial temperature. The last gives +3.0 mm for a 75 °C start, against the nonlinear 3.4 mm of Table 6.6. The heat share dominates the design variable; convection barely moves it.

Identifiability from bench data

For measurements $\boldsymbol{y} = \boldsymbol{h}(\boldsymbol{\theta}) + \boldsymbol{\epsilon}$ with $\boldsymbol{\epsilon} \sim \mathcal{N}(0, \sigma^2 I)$, the Fisher information and the Cramér–Rao bound are

$$F = \frac{1}{\sigma^2} S^{\mathsf{T}} S, \quad S = \frac{\partial \boldsymbol{h}}{\partial \ln \boldsymbol{\theta}}, \qquad \operatorname{cov}(\hat{\boldsymbol{\theta}}) \geq F^{-1}. \tag{B6.16}$$

Take $\boldsymbol{\theta} = (\beta, h_v, G_{sc})$ for the 160 mm rotor, samples every 0.5 s up to 60 s and $\sigma = 2$ K. A single peak temperature gives rank $F = 1$, so three parameters cannot be identified from it (Section 6.6).

Data	σ_β	σ_{h_v}	σ_G	$\rho(\beta, G)$
Track history	0.58%	17.6%	0.82%	0.59
Track and core	0.47%	14.8%	0.40%	0.31

A core thermocouple halves the uncertainty of G_{sc} and halves its correlation with β. The correlation $\rho(\beta, h_v)$ stays at 0.991–0.995, however, because in a single stop the convective loss is a small, almost proportional correction to the stored heat. Separating β from h requires different airflows or power histories, as proposed in Sections 6.6 and 7.2. These local bounds assume a correct model structure; model error has to be judged on held-out tests.

6.6 Numerical verification and model identification

The Python model integrates the temperatures and the convective and radiative energies with an adaptive Runge–Kutta solver. Appendix B provides a closed-form constant-convection verification and an energy closure check. These verify the numerical calculation under its governing equations. The friction map and thermal parameters still need measured quantities before absolute temperatures or repeat braking can be claimed. Separate measurement of torque and speed sets wheel input power. Disc and pad temperatures, cooldown at multiple airflow conditions and the temperature difference between rotor locations help separate the heat split, external exchange and internal conductance. A single maximum surface temperature would leave these parameters correlated.

7. Engineering disposition and verification

7.1 Conditional selection

The reference stop sets a common demand of 3.14 kN at the braked axle and 551 kJ of work per wheel. It gives 260.7 N·m at the unloaded drawing radius, with a clear dependency on actual loaded radius. A coherent wheel-end specification has to use the same effective radius, corner loads and temperature history through the structural, caliper and thermal checks.

Table 7.1 – Conditional decision for the three studied envelopes.

Candidate	Decisive evidence	Disposition
160 mm drawing	Diameter exceeds the 125 mm cap by 35 mm. Track is 390 °C in the reference case and 452 °C at lower coupling.	Retain as a comparison datum.
125 mm, comparable relief	Bulk 534 °C and track 579 °C at 22 mm. Requires 336 bar at $\mu = 0.15$.	Investigate heat capacity, heat split and piston/track trade-offs together.
125 mm solid bound	Mass rises to 1.980 kg. Bulk 455 °C and track 506 °C at 22 mm.	Use as a maximum-mass check for the studied envelope.

The 160 mm drawing provides an architectural reference for the rotor, caliper and hub. It is outside the published diameter cap. The capped cases quantify how its smaller radius and mass change two different limits. The 125 mm rotor needs higher pressure at the same pad friction. Under the reference heat share, the 22 mm mass envelope also exceeds the source's track-temperature comparison. Carrying forward the 125 mm constraint therefore requires reconsidering available thermal mass, heat partition and hot friction together. If the true wheel or caliper geometry admits a revised diameter, that change requires a documented requirement revision.

The axle and clamped interfaces require the actual load paths as well as matching parts lists. The radial force path can be evaluated with the bearing centres located from the selected catalogue parts. The caliper reaction path determines the torque share of the axle. The rotor and rim fasteners require independent friction-joint or positive-drive definitions. The sensitivity results identify which dimensions and component characteristics to establish before selecting production hardware and setting preload.

7.2 Verification sequence

A useful development sequence establishes installation envelope, rolling radius, bearing geometry, hot torque and transient temperature before evaluating fatigue or repeated stops. Table 7.2 links measurable quantities with design decisions. Braking energy can be verified against torque times angular speed integrated on a brake rig. A subsequent thermal fit should use several power histories and airflows, preserving separate cases to

Box 7.1 Uncertainty propagation and global sensitivity of the thermal verdict

Theoretical complement to Sections 7.1–7.2. Monte Carlo on the two-node model of Section 6.3, computed by brake_theory.py (Appendix D); the input ranges are those of Tables 6.1 and 6.5 plus the brake share of Section 2.2.

Probabilistic formulation

The deterministic verdict of Table 7.1 compares one track-node peak with 450 °C. To see how robust it is, treat the uncertain inputs as independent random variables,

$$\beta \sim \mathcal{U}(0.60, 0.95), \quad h_v \sim \mathcal{U}(50, 400),$$
$$\ln G_{sc} \sim \mathcal{U}(\ln 45, \ln 180), \quad \varepsilon \sim \mathcal{U}(0.5, 0.9),$$
$$\lambda \sim \mathcal{U}(0.50, 0.60), \tag{B7.1}$$

where the heat input of the more loaded brake scales as $2\lambda\beta P_w$, and take $Y = \max_t T_s(t)$ as the response. The exceedance probability and its Monte Carlo estimate are

$$p_f = \Pr(Y > T_{\lim}), \qquad \hat{p}_f = \frac{1}{N}\sum_{i=1}^{N} \mathbb{1}[Y_i > T_{\lim}], \tag{B7.2}$$

with standard error $\sqrt{\hat{p}_f(1-\hat{p}_f)/N}$. The distributions express the present state of knowledge, so p_f measures how strongly the verdict depends on the assumed ranges. It is not a field failure rate.

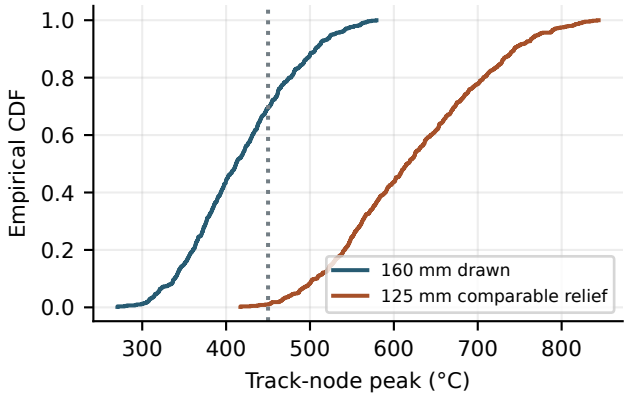

Empirical distribution of the track-node peak, $N = 600$ samples per rotor. Dotted line: 450 °C comparison.

Rotor	mean ± sd (°C)	5/50/95% (°C)	$\hat{p}_f$
160 drawn	418 ± 64	319 / 412 / 528	0.307 ± 0.019
125 relief	623 ± 90	487 / 617 / 773	0.992 ± 0.004

The 125 mm rotor with comparable relief exceeds the comparison temperature for almost every admissible input. The drawn rotor does so in about a third of the cases. A normal approximation, $p_f \simeq \Phi_N[(\mu_Y - T_{\lim})/\sigma_Y]$, gives 0.307 and 0.972. The second value underestimates the empirical 0.992 because the response is right-skewed.

Variance-based sensitivity

The Hoeffding–Sobol decomposition splits the output variance into contributions of single inputs and their interactions:

$$\operatorname{Var} Y = \sum_i V_i + \sum_{i<j} V_{ij} + \ldots, \qquad S_i = \frac{\operatorname{Var}(\mathbb{E}[Y \mid X_i])}{\operatorname{Var} Y}. \tag{B7.3}$$

When a linear regression on the standardised inputs explains most of the variance (R^2 close to 1), the first-order indices reduce to the squared standardised regression coefficients,

$$S_i \simeq \mathrm{SRC}_i^2, \qquad \mathrm{SRC}_i = b_i \sigma_{X_i}/\sigma_Y. \tag{B7.4}$$

Here $R^2 = 0.973$ and 0.972, and $\sum_i \mathrm{SRC}_i^2 = 0.977$ and 0.976.

$S_i \simeq \mathrm{SRC}_i^2$	β	G_{sc}	λ	h_v	ε
160 drawn	0.62	0.24	0.10	0.009	$< 10^{-4}$
125 relief	0.72	0.13	0.12	0.012	$< 10^{-3}$

The rotor heat share explains 60–70% of the variance, internal conduction 13–24% and the brake balance 10–12%. Convection and emissivity are negligible over one stop. The ranking agrees with the implicit sensitivities and the identifiability analysis of Box 6.3. It gives a quantitative order for the measurements of Table 7.2: rig torque and temperature to fix β, then multi-depth temperatures for G_{sc}, then the corner loads that set λ. Airflow matters later, for repeated stops and recovery.

check prediction. Adding stall or thermal-soak conditions would exercise the fluid and pad temperature channels alongside the rotor.

Table 7.2 – Measurements for the next design iteration. The order starts from the interfaces that determine all downstream models.

Test or input	Observable	Model decision
Packaging and wheel geometry	Loaded radius, track radii, caliper and mounting envelopes	Resolve diameter and force-to-torque conversion
Corner-load measurements	Braked-axle weight and load transfer, longitudinal and side loads	Resolve grip, bearing reactions and axle load envelope
Brake hardware inspection	Bearing catalogue IDs, measured endplay and preload, bolt sizes and contact surfaces	Resolve pair life and clamped-joint slip
Caliper and rotor bench data	Pressure, torque, speed, track and core temperatures, recovery	Identify μ, β, h and effective track-to-core exchange
Structural model and test	Section stress or strain, stiffness, fillet geometry, joint deformation	Verify force paths. Quantify factors, fatigue and robustness.

For installation decisions, the load envelope also includes potentially asymmetric brake balance, aerodynamic terms where applicable and changes in normal load through the ground roll. Failure conditions and the energy capacity of the actual installed system belong to the applicable certification basis [2]. The present calculations support the earlier concept-screening stage and prioritise the data required to revisit the design.

7.3 Conclusion

The main relationship exposed by the comparison is that reducing the rotor diameter at constant package thickness raises both the hydraulic pressure for a given torque and the transient temperature for a given wheel work. In the comparable-relief model the move from 160 to 125 mm reduces mass from 2.791 to 1.658 kg. It increases pressure at μ = 0.30 from 130 to 168 bar in the assumed track geometry, and the cold track peak from 390 to 579 °C at the reference energy partition. The capped solid bound still reaches 506 °C at the track. At 125 mm, the next design decision depends chiefly on admissible mass and thermal geometry, verified pad friction when hot, and the actual load transmitted into the shaft, bearings and joints.

References

[1] D. Kumar and A. Azzouz. *Étude et conception d’un système de freinage d’avion léger*. Technical design dossier, UE COSA, Arts et Métiers, Paris, academic year 2024–2025, 18 pp. Unpublished. Assembly and disc drawings dated 9 January 2025.

[2] European Union Aviation Safety Agency. *Easy Access Rules for Normal-Category Aeroplanes (CS-23)*, Amendment 6, CS 23.2305 “Landing gear systems”, 2026 consolidated edition. EASA reference.

[3] SKF. *Tapered roller bearings*. In *Rolling bearings catalogue*, ch. 8, pp. 681–682, Table 7. Catalogue chapter.

[4] International Organization for Standardization. *Rolling bearings — Dynamic load ratings and rating life*. ISO 281:2007, Geneva. Standard record.

[5] R. T. Barrett. *Fastener Design Manual*. NASA Reference Publication 1228, Lewis Research Center, 1990. NASA Technical Reports Server.

[6] J. H. Lienhard V and J. H. Lienhard IV. *A Heat Transfer Textbook*, 6th ed., 2024. Textbook and publication information.

[7] M. P. Dyko and B. T. F. Chung. *Finite Element Thermal Model of an Aircraft Wheel and Carbon Brake Assembly*. SAE Technical Paper 901909, 1990. 10.4271/901909.

Appendix A. Source dossier and assembly sequence

The technical sheets of [1] describe the architecture, proposed forces and preload, shaft, rim/disc joint, rotor heating, caliper and assembly. Table A.2 records the numerical and configuration changes needed to make those sheets comparable under one mission model.

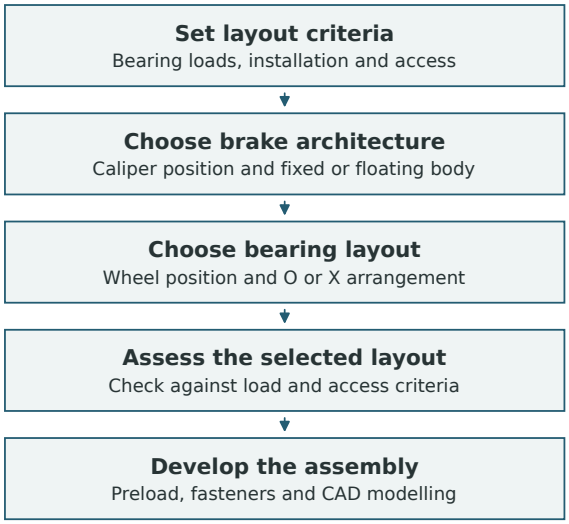

Figure A.1 – Methodology from [1, p. 4], redrawn in English for this report. The original sequence is retained.

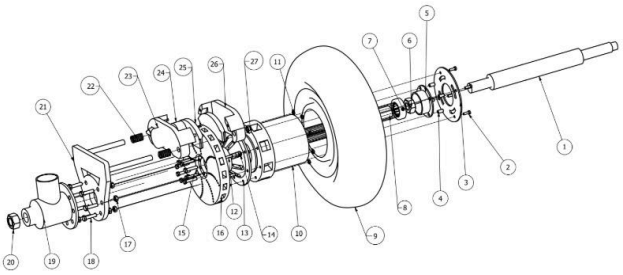

Figure A.2 – Original assembly view from [1, p. 14]. For the exploded detail and part references see Plate C.1.

Table A.1 – Assembly sequence recorded in the original report, pp. 14–15 [1]. Fastener designations follow that source.

Steps	Operations in archived order
1–3	Install airframe connection. Locate the axle. Tighten the axle with the M18 nut.
4–6	Fit the caliper base. Bolt it to the airframe connection with seven fasteners. Fit two return springs.
7–10	Fit the moving caliper body, piston, first pad and disc in that order.
11–12	Fasten the disc-side link with eight M5 fasteners. Fit the intermediate wheel connection with eight M6 fasteners.
13–16	Fit first roller bearing, spacer and second roller bearing. Tighten the M18 axle nut.
17–18	Fit the second side of the caliper with the second pad. Tighten the moving caliper assembly using two M8 nuts.
19–22	Fit the wheel and tire. Fit cap 1. Attach cap 1 with four M5 screws. Install cap 2 with four M6 screws.

Table A.2 – Traceability from the archived calculation sheets to the revised analysis. Original quantities are reported for comparison.

Source	Recorded claim or input	Treatment in this report
pp. 3, 18	Maximum Ø125 mm and drawn Ø160 mm	Keep the requirement, compare the two envelopes, flag configuration control (Sec. 1).
p. 7	2,740 N axial load, 456.7 N per bearing and 357 N from a factor of 1.6	Rotate the force to the correct plane, distinguish external axial force and induced thrust, check arithmetic (Sec. 3).
pp. 8–10	Limit 140 MPa, factor two, fillet stresses 195 and 270 MPa	Separate shear and equivalent stress. Restore torsional gradient and fourth-root bending law (Sec. 4).
p. 11	204 N·m, 256 N, 5,329 N, 4.14 N·m and 241 MPa	Retain the nominal torque check, split friction slip, bearing pressure and fastener preload models (Sec. 4).
p. 12	2.791 kg, 530 kJ input, 470 kJ dissipated, 38 s	Derive aircraft work and distinguish frictional heat, storage and time-dependent cooling (Sec. 6).
p. 13	280 bar, 13 mm and around 15 kN	Recover the piston force and propagate pressure and friction to torque (Sec. 5).
pp. 14–18	Assembly steps, wheel/axle and rotor plans	Preserve sequence and native technical illustrations (Appendices A and C).

The assembly sequence follows the archived description and explains the design intent. The fastener and tightening identifiers in the written sequence and drawing require a common revision before they can specify any physical build. Table 4.2 gives the directly identifiable differences.

Appendix B. Reproducible numerical model

B.1 Files and environment

The embedded archive **Frein_Avion_Reproduction.zip** contains **brake_study.py**, a dependency list, the generated tables in **study_results.json**, and vector plots. The runs in the report used Python 3.12.14, NumPy 2.3.5, SciPy 1.17.0 and Matplotlib 3.10.8. There is no random input or external simulation package. The dossier values used by the code and the added model inputs are listed in Sections 1, 2 and 6. Extract the archive from the PDF's attachments in a reader that supports PDF attachments.

```
python -m pip install -r requirements.txt
python brake_study.py --out results
```

The calculation first sets the wheel force and power, creates the traction and mechanical screens analytically, and then integrates the thermal equations. A vectorised parameter sweep uses 41 initial convection coefficients and 47 heat partitions for each diameter. It computes additional warm starts and three thermal conductances. A Brent root solver inverts the peak-temperature calculation at 125 mm for thickness or heat partition. The PDF figures are generated directly from those model runs.

B.2 Closed form in the linear thermal limit

A verification case sets constant h, ignores radiation and uses one heat capacity $C=M_d c_p$. With $u=T-T_a$, $u(0)=0$, $k=hA/C$ and $\alpha=\beta P_w(0)/C$, the equation and verification solution over the braking interval are

$$\dot{u} + ku = \alpha(1 - t/t_s), \tag{B.1}$$

$$u = \alpha\left[z - \frac{t - z}{k t_s}\right], \qquad z = \frac{1 - \exp(-kt)}{k}. \tag{B.2}$$

Equation (B.2) follows by multiplying (B.1) by the integrating factor exp(kt). With vanishing cooling, $z=t-kt^2/2+O(k^2)$ and u tends to $\alpha(t-t^2/(2t_s))$. The deterministic comparison for the 160 mm scenario uses 251 sample times and gives a

maximum difference of about 1.6×10^{-9} °C between the linear analytical solution and the dedicated high-accuracy numerical solve.

B.3 Thermal energy closure

The transient model integrates $E_i=\int Q_i\,dt$ jointly with each temperature. Cancelling internal exchange gives the same energy balance for both networks.

$$\beta W_{b,w} = \sum_i C_i(T_i - T_{i,0}) + E_{\mathrm{conv}} + E_{\mathrm{rad}}. \tag{B.3}$$

The reference traces, including the additional cooldown interval, close within 0.009 J in the larger of the one- and two-node residuals. The ordinary simulations use a relative integration tolerance of 2×10^{-9}, absolute tolerance 5×10^{-8}, and retained samples at most 0.05 s apart during the stop. The deceleration sweep samples every 0.10 s. Peaks and first crossing times refer to the reported sampling. Conservation and the linear limit check numerical implementation. Comparisons to test data would address the adequacy of the model coefficients.

Appendix C. Technical drawings

The three landscape sheets reproduce the original CAD plans [1, pp. 16–18] at their original A3 sheet size. Their drawing scales apply at that size. The original French labels and date of 9 January 2025 have been retained. The sheets document the design configuration used for comparison.

Plate C.1 shows the exploded wheel-end assembly and parts list. It includes the carrier, caliper, support, wheel, tapered roller bearings and joint hardware.

Plate C.2 gives orthogonal and section views of the assembly, including the bearing stack and spacer annotations in H–H. The loaded tire radius for mission calculations is a separate input.

Plate C.3 gives the rotor external diameter, height, centre features and hole layout of the drawn configuration. The 160 mm callout is the origin of the diameter comparison in Section 1.

Appendix D. Theory supplement

Nine theory boxes, inserted after the pages they complement, derive the models of Sections 2–7 and add closed forms, bounds and simulations. The conclusions of the main text do not depend on them. Their numbers are produced by *brake_theory.py*, attached to this PDF together with its output *brake_theory_results.json*. The script reuses the inputs of *brake_study.py*, adds the assumptions marked as illustrative in each box and draws the five box figures.

It needs NumPy, SciPy and Matplotlib only, and its Monte Carlo stream is seeded. Closed forms are checked by direct computation: the Crank–Nicolson track model against the constant-flux and Duhamel solutions (B6.4), the track–core difference (B6.9) against integration of (6.5)–(6.6), and the inverse sizing against Table 6.6.

```
python brake_theory.py --out theory
```

Plate C.1 | Exploded assembly and parts list

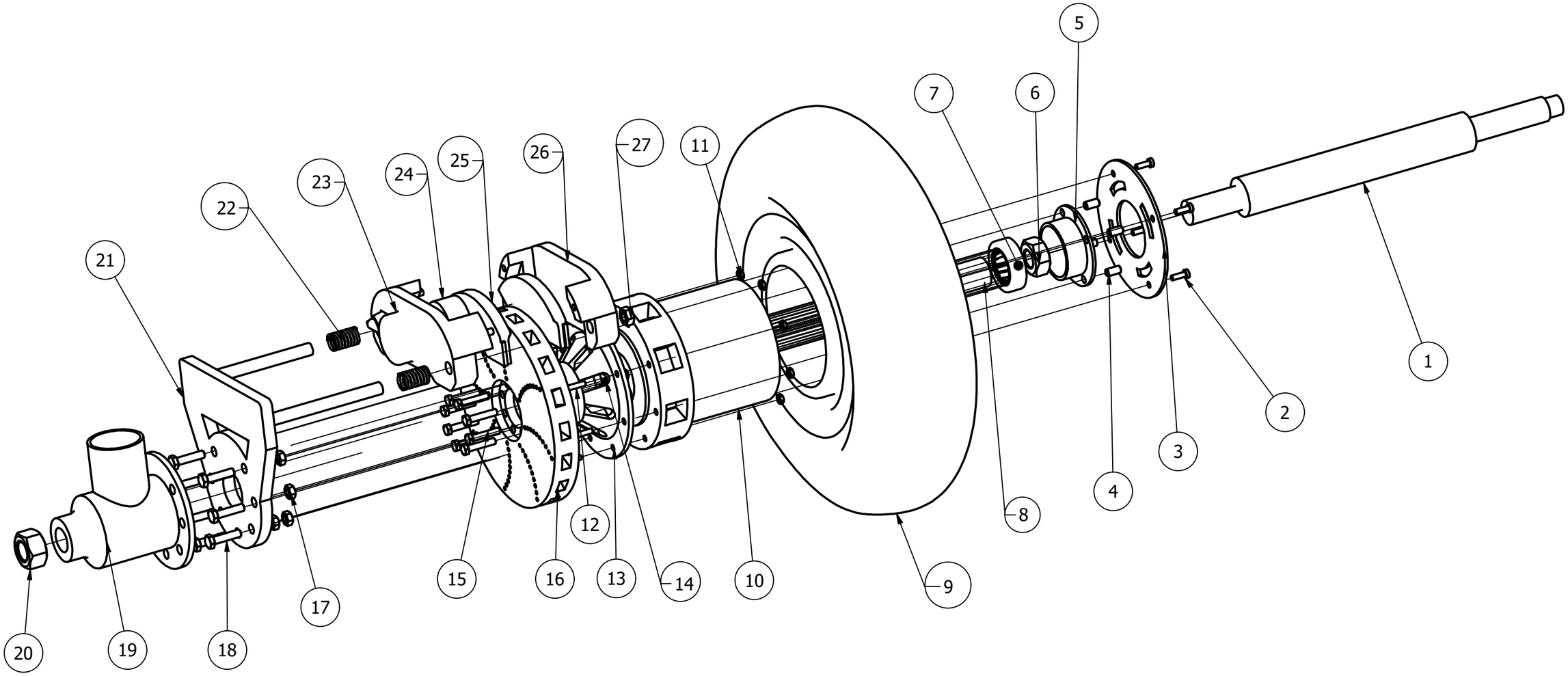

Tableau des elements		
Nomenclature	Quantite	Pièce
1	1	Axe
2	4	Vis de maintien du chapeau 1 (M6 x 25)
3	3	Chapeau 1
4	4	Vis de maintien du chapeau 2 (M6 x12)
5	1	Chapeau 2
6	1	Ecrou de maintien de l'axe
7	2	Roulements coniques
8	1	Entretoise de precontrainte
9	1	Roue + Jante
10	1	Pièce intermediaire
11	8	Ecrou disque-jante (M6)
12	8	Vis disque-jante (M6 x 16)
13	1	Liaison disque-jante
14	8	Ecrou disque-liaison (M6)
15	8	Vis disque-liaison (M6 x 25)
16	1	Disque
17	7	Ecrou etrier-liaison avion (M6)

Nomenclature	Quantite	Pièce
18	7	Vis etrier-liaison avion (M6 x25)
19	1	Liaison avion
20	1	Ecrou serrage liaison avion (M18)
21	1	Support etrier
22	2	Ressort du rappel
23	1	Etrier mobile
24	1	Piston
25	2	Plaquettes
26	1	Etrier fixe
27	2	Ecrou serrage etrier (M8)

Dessinateur:
KUMAR Dev
AZZOUZ Amir

ARTS ET MÉTIERS ParisTech

ENSAM
Concevoir Système

Projet:
CONCEPTION DU FREIN A DISQUE MOBILE

Système:

Echelle: 1/1

Unites: mm

Format: A3

Date: 09/01/25

Plan: ENSEMBLE DU FREIN

Plan ID: IDENTIFICATION DES ELEMENTS

Plan: 1/3

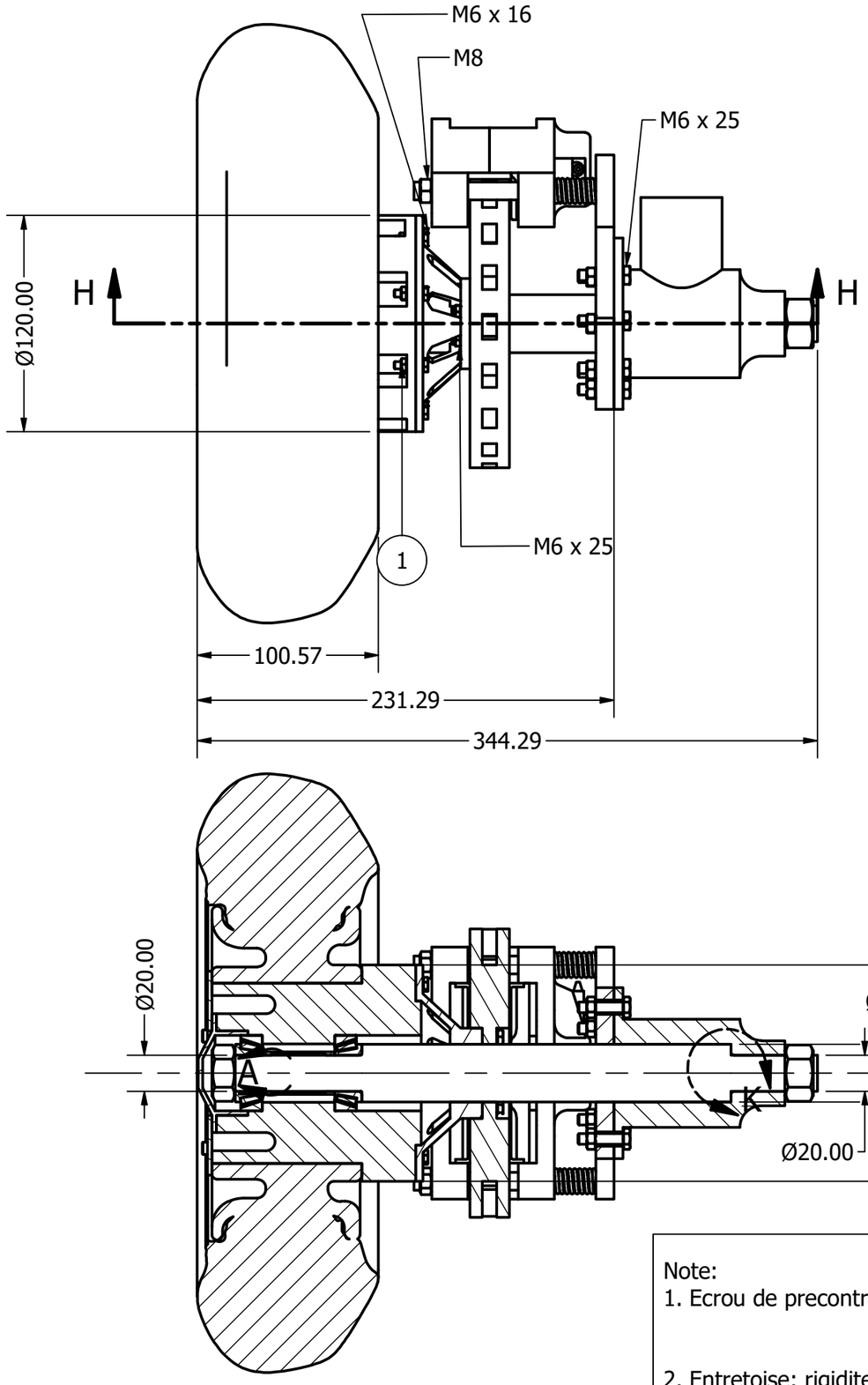

SECTION H-H
ECHELLE 1 / 3

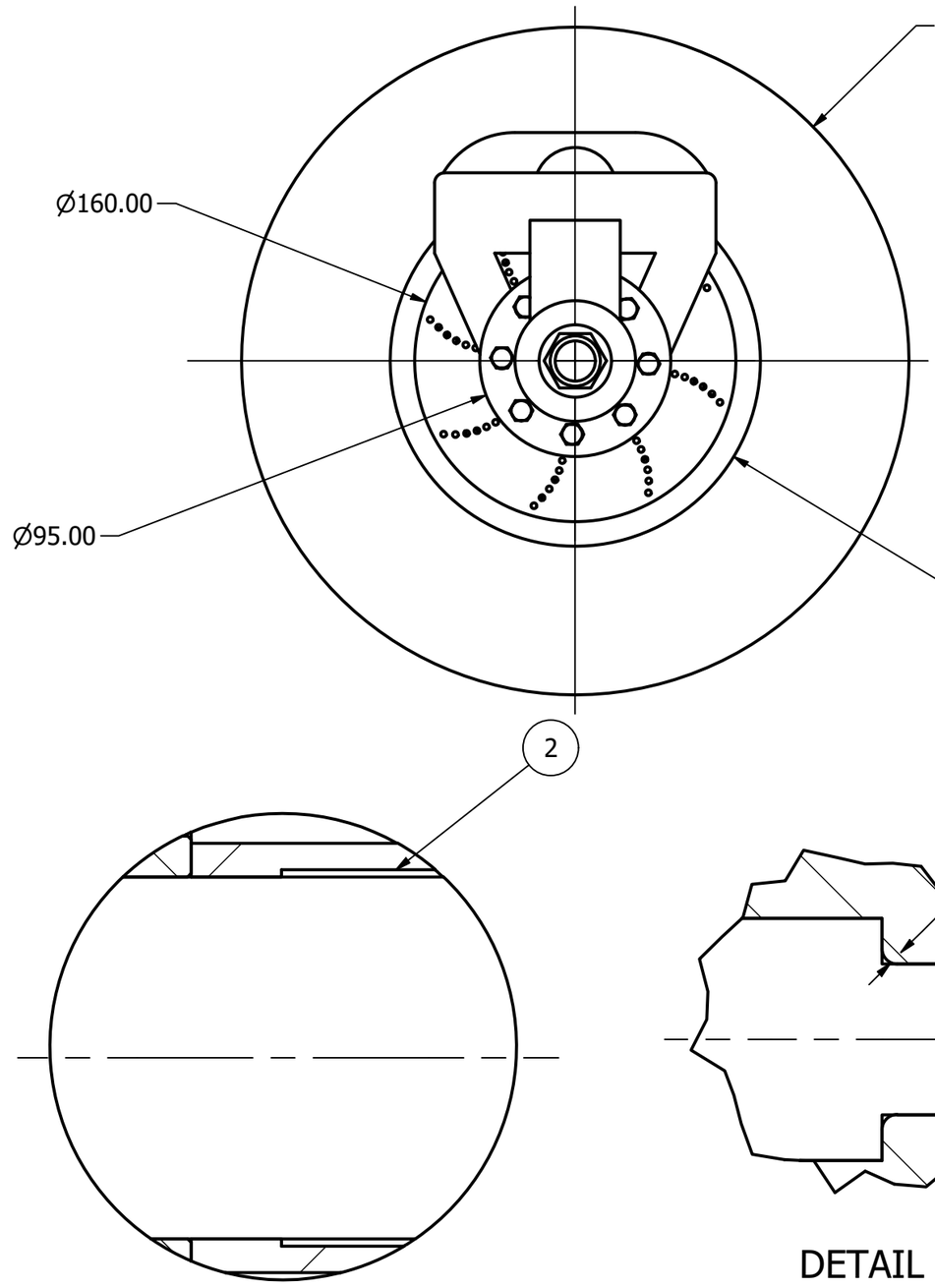

DETAIL A

DETAIL K

Note:
1. Ecrou de precontrainte:couple - 4.14 N/m-cB
precontrainte -5329N

2. Entretoise: rigidite axiale - 159 MN/m
rigidite radiale - 157 MN/m
u = 0.1 mm

Dessinateur: KUMAR Dev, AZZOUZ Amir		ENSAM Concevoir Système	
		Projet: CONCEPTION DU FREIN A DISQUE MOBILE	
Système:	Echelle: 1/3	Unites: mm	Plan: ENSEMBLE FREIN A DISQUE MOBILE
	Format: A3	Date: 09/01/25	
			Plan ID: DIMENSIONNEMENT GENERAL — Plan: 2/3

Plate C.3 | Rotor geometry

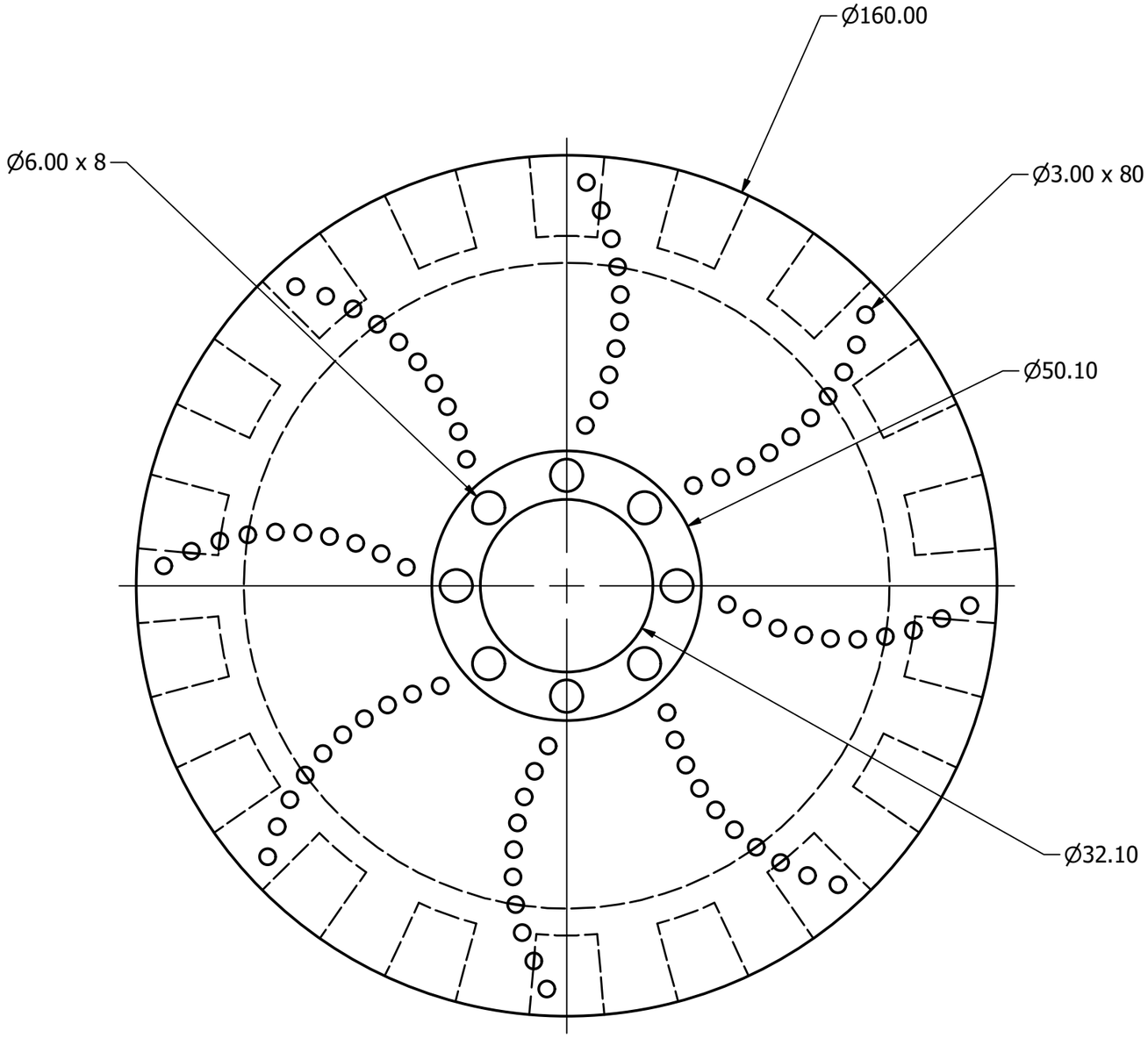

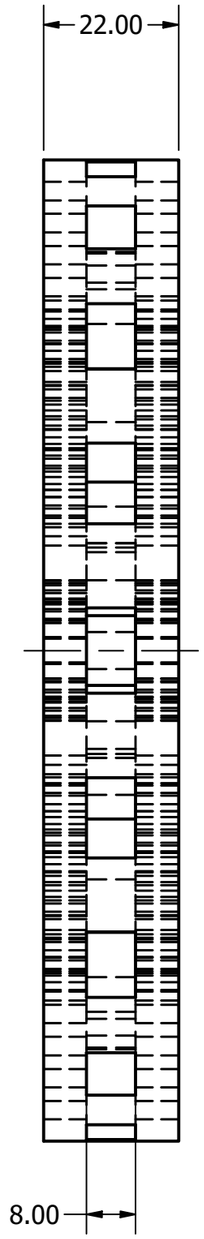

Dessinateur: KUMAR Dev, AZZOUZ Amir		ENSAM Concevoir Système	
		Projet: CONCEPTION DU FREIN A DISQUE MOBILE	
Système:	Echelle: 1/1	Unites: mm	Plan: DISQUE
	Format: A3	Date: 09/01/25	
		Plan ID: DIMENSIONNEMENT DISQUE	Plan: 3/3